Experimental Thermal and Fluid Science 172 (2026) 111659

Contents lists available at ScienceDirect

Experimental Thermal and Fluid Science

journal homepage: www.elsevier.com/locate/etfs

Multi-domain investigation of combustion instability in gas turbine engines using a uniaxial MEMS piezoelectric accelerometer

P.Di Gloria [a,*], M.G.De Giorgi [a], M.A. Signore [b], L. Francioso [b]

[a] Department of Engineering for Innovation, University of Salento, Lecce, Italy
[b] CNR IMM, Institute for Microelectronics and Microsystems, Via Monteroni, Lecce I-73100, Italy

A B S T R A C T

This work presents a multi-domain experimental characterization of combustion instabilities in a liquid-fueled swirling combustor operating with Jet-A1, combining high-speed optical imaging, dynamic pressure measurements, and structural vibration monitoring. Experiments were conducted at two global equivalence ratios ($\Phi = 0.36$ and $\Phi = 0.18$), representative of stable and ultra-lean unstable operating conditions. Flame dynamics were analyzed using Proper Orthogonal Decomposition (POD), Spectral POD (SPOD), and Cross-Fourier Transform (Cross-FFT), while pulsation mechanics were investigated through the Autocorrelation Function (ACF). Pressure fluctuations and structural vibrations were monitored using a commercial pressure sensor and an innovative uniaxial AlN-based piezoelectric MEMS accelerometer, fabricated via CMOS-compatible processes and characterized in terms of sensitivity, linearity, resonance, and hysteresis. Time-domain analysis revealed increased signal dispersion and intermittency at $\Phi = 0.18$, while frequency-domain analysis showed that the MEMS accelerometer effectively captures transient components between 156 and 625 Hz, typical of turbulent combustion. Cross-spectral analysis demonstrated high coherence between accelerometer signals and dominant flame modes, highlighting the sensor's capability to monitor structural dynamics and localized instabilities in real time. The results confirm that the MEMS accelerometer is a compact, non-intrusive, and reliable tool for real-time diagnostics of thermoacoustic instabilities, which can be integrated with optical and pressure measurements for advanced monitoring and control strategies. This combined approach offers valuable perspectives for developing advanced monitoring strategies and real-time control of gas turbine combustors.

1. Introduction

The study of combustion instabilities is crucial for the development of efficient and reliable combustion systems. These instabilities, often manifested as pressure oscillations and structural vibrations, can significantly affect the performance and safety of propulsion and power generation systems [1,2]. If not properly controlled, they can cause excessive thermal loads, increased emissions, and, in the most extreme cases, catastrophic structural failure [3,4].

Traditional monitoring techniques mainly rely on pressure transducers, but recent advancements in piezoelectric accelerometers offer a promising alternative for detecting combustion-induced vibrations, thanks to their high sensitivity and wide frequency bandwidth [5,6]. In particular, piezo-MEMS accelerometers manufactured using standard CMOS processes are gaining increasing interest for their compact size, integration capability, and robustness in extreme environments [7,8]. A miniaturized piezoelectric MEMS accelerometer with a polygonal topology has been developed with an area of only $868 \times 833\ \mu m^2$, using six trapezoidal cantilevers with shorter fixed sides to improve tension sensitivity. Made on Cavity-SOI substrates with a thin aluminum nitride (AlN) film of approximately 928 nm, it exhibited a natural frequency of 98 kHz and a sensitivity increase of 22.48 % compared to traditional trapezoidal cantilevers [9]. Shi et al. [10] developed a piezoelectric MEMS accelerometer (PMA) for vector hydrophones, featuring a four-beam cantilever structure integrated with an inertial mass, characterized by light weight and high sensitivity. Made on a silicon substrate with thin PZT films, it demonstrated a resonance frequency of 2300 Hz and excellent resistance to interference, proving ideal for vector hydrophone applications with a sensitivity of −178.99 dB@1000 Hz and a bandwidth of 20–1100 Hz. Additionally, piezoelectric MEMS accelerometers with a trampoline structure and annular diaphragm were designed using PZT-5H and COMSOL Multiphysics to achieve low transverse sensitivity along one axis and good thermal stability. These devices were integrated into ASIC circuits and RF telemetry systems for wireless monitoring of industrial equipment. [11].

The piezoelectric accelerometer measurements provide valuable insights into the vibrational characteristics of combustion instability, while imaging techniques, such as luminance analysis, offer a complementary view of the flame's temporal evolution. By combining accelerometric data with high-speed imaging, a more comprehensive understanding of the spatial and temporal dynamics of the flame and its interaction with combustion-induced vibrations can be achieved.

Additionally, applying instantaneous time series analysis to

* Corresponding author.
E-mail address: pasquale.digloria@unisalento.it (P.Di Gloria).

https://doi.org/10.1016/j.expthermflusci.2025.111659
Received 9 July 2025; Received in revised form 5 November 2025; Accepted 12 November 2025
Available online 16 November 2025

Nomenclature

ACF	Autocorrelation Function
AlN	Aluminum Nitride
ASIC	Application Specific Integrated Circuit
BOE	Buffered Oxide Etchant
CMOS	Complementary Metal-Oxide-Semiconductor
CRZ	Combustion Recirculation Zone
ESPRIT	Estimation of Signal Parameters via Rotational Invariance Technique
FFT	Fast Fourier Transform
I.C.E.	Internal Combustion Engine
ICP	Inductive Couple Plasma
LBO	Lean Blowout
LSTM	Long Short-Term Memory
MEMS	Micro Electro-Mechanical Systems
PDF	Probability Density Function
POD	Proper Orthogonal Decomposition
PMA	Piezoelectric MEMS Accelerometer
PZT	Lead Zirconate Titanate
RF	Radio Frequency
SiO_2	Silicon Oxide
SOI	Silicon-On-Insulator
SPOD	Spectral Proper Orthogonal Decomposition
Φ	Global equivalence ratio

luminance images enables a deeper exploration of flame instability, revealing how fluctuations in brightness over time correlate with the evolving combustion process [12].

Dynamic correlation analysis has been used to examine the relationship between pressure and acceleration signals in combustion systems, providing insights into the coupling mechanisms between acoustic waves and structural vibrations [13]. For example, Barelli et al. [14] proposed a diagnostic methodology for monitoring combustion quality in internal combustion engines (I.C.E.) using non-invasive measurements, such as acoustic and vibration signals, correlated with the indicated mean effective pressure. Their experimental campaign demonstrated that signals measured on the cylinder head strongly correlated with in-cylinder phenomena, depending on engine load and combustion frequency. These approaches highlight the potential of combining accelerometric and imaging data to better understand combustion instability, offering a more comprehensive view of the dynamic interaction between flame behavior and vibrations within the combustion chamber.

Recent research has demonstrated that strong correlations can be established between the dynamic signals recorded by fast-response pressure sensors and structural vibrations measured via accelerometers. For example, Giuliani et al. [15] combined optical, acoustic, and pressure sensing to monitor combustion in a gas turbine, highlighting how accelerometers and pressure probes can capture combustion instabilities effectively. Seongpil et al. [16] employed dynamic pressure signals to diagnose combustion instability in a gas turbine combustor, proposing a novel methodology based on the zero-crossing rate. Similarly, Jongwun et al. [17] also used dynamic pressure to evaluate two diagnostic methods for combustion instability based on the concept of entropy, using experimental data from a gas turbine combustor. Kefalas et al. [18] proposed a method using discrete wavelet transform and gradient boosting to estimate combustion parameters from vibration data, with proven correlations to in-chamber pressure measurements.

Lengani et al. [19] provided valuable insights into the use of accelerometers and pressure sensors during unstable combustor operations in industrial gas turbines, showing clear signal correlations and effective detection of instability onset. Furthermore, Giuliani et al. [20] used multiple transducers to monitor dynamic flame behaviors, reinforcing the role of synchronized pressure and vibration sensing in combustion diagnostics.

In terms of sensor reliability and application in harsh turbine environments, Mevissen and Meo [21] reviewed various sensor technologies used for non-destructive testing and structural health monitoring of hot gas components, underlining the role of accelerometers and pressure sensors. The trend is toward smart integration, as seen in Nicchiotti et al. [22] who validated an optical pressure sensor alongside accelerometers in a turbine setup, suggesting multi-sensor configurations enhance combustion monitoring under transient load conditions.

This synergy between pressure and vibration-based data not only improves combustion parameter estimation but also supports predictive maintenance and early fault detection. As a result, these sensor technologies are paving the way for more intelligent gas turbine diagnostics and control strategies.

Statistical measures such as variance and kurtosis are commonly used to gauge combustion stability. In this context, Osama et al. [23] propose a parametric subspace estimator—ESPRIT—augmented with kurtosis-based selection to identify dominant modes in droop-controlled microgrids. ESPRIT exploits the rotational invariance of the signal subspace to return model-based estimates of frequency (and, when formulated, damping) that are far less sensitive to window length, leakage, and bin resolution than non-parametric spectra (e.g., FFT/periodogram). It can separate closely spaced tones under moderate SNR where classical methods smear peaks, because it uses a noise/signal subspace decomposition rather than peak picking on a discretized spectrum. The kurtosis stage acts as a robust discriminator: by emphasizing non-Gaussian, intermittent components relative to quasi-Gaussian background fluctuations, it improves mode order selection and suppresses spurious estimates induced by broadband noise. Together, the subspace formulation (which provides asymptotically unbiased, high-resolution estimates when the model order is correctly chosen) and the kurtosis filter (which stabilizes the estimator in noisy or time-varying conditions) explain the higher accuracy and robustness reported by the authors relative to conventional FFT-based or purely non-parametric approaches. The Fast Fourier Transform (FFT) remains useful here as a complementary tool to visualize the overall spectral content and to initialize frequency bands for subsequent parametric refinement [24].

For example, as demonstrated by Tarun et al. [25], by coupling FFT and POD analyses, it was possible to identify the dominant instabilities associated with the supersonic flow over aerodynamic cavities, experimentally investigated to reduce unwanted oscillations. To extend this analysis, the Cross-Fast Fourier Transform (Cross-FFT) is used to explore the correlation between frequency components from different datasets, particularly between the eigenvalues extracted from the Proper Orthogonal Decomposition (POD) applied to luminance images and the corresponding pressure or acceleration signals [26].

This cross-spectral framework enables a more nuanced interpretation of combustion dynamics by identifying frequency-aligned phenomena across different sensing modalities. Furthermore, several alternative spectral estimation methods have been developed—many of which became computationally viable following the introduction of the FFT algorithm—offering a compelling balance between accuracy and computational efficiency [27]. For example, Zheng et al. [28] leverage FFT to accelerate mass spectrum alignment via cross-correlation, demonstrating the algorithm's versatility in signal processing applications.

Following the frequency-domain and statistical approaches, advanced time–frequency and modal decomposition techniques such as

Spectral Proper Orthogonal Decomposition (SPOD) are applied to luminance images to study combustion structures within the frequency bands identified via Cross-FFT, revealing coherent flame dynamics and mode interactions [29,30]. Wavelet analysis is widely used to study transient phenomena in pressure and acceleration signals, allowing for the capture of localized variations in time–frequency space. This approach is particularly useful for detecting intermittency phenomena and mode transitions in combustion instabilities [31,32]. Furthermore, Wavelet analysis is applied to the analysis of disturbance fields composed of vibrations. The propagating waves exhibit varying amplitudes, frequencies, speeds, and directions. Wavelet analysis, by associating temporal information with frequency content, enables the identification of symmetric and antisymmetric waves, as well as reflection and dispersion phenomena [33]. In the context of online monitoring and fault diagnosis in altitude simulation equipment, Wavelet analysis combined with an LSTM neural network was proposed by Zhi-Hong et al. [34] for the diagnosis of sensors in an inlet pressure modulation system. Wavelet analysis extracts features such as the modulus maximum and high-frequency energy, improving signal discrimination. The LSTM neural network, trained with sensor feature data under different pressure conditions, enables fault diagnosis and accurately predicts random failures of a pressure sensor.

Existing studies show that pressure transducers and conventional accelerometers can reveal thermoacoustic behavior, but three gaps remain for swirl-stabilized, liquid-fueled combustors near lean blowout: limited in-situ validation of CMOS-compatible piezo-MEMS devices against pressure and flame imaging; insufficient discrimination between phase-locked limit cycles and blowout-driven, intermittent dynamics using consistent, multi-indicator criteria; and scarce modality fusion that links sensor signals to coherent flame structures via POD/SPOD coupling. This work addresses these gaps by proposing a robust, sensor-fusion methodology centered on piezoelectric accelerometry and advanced decomposition techniques. A monolithically integrated AlN piezo-MEMS accelerometer (standard CMOS-compatible process) is deployed alongside a reference pressure transducer and high-speed imaging at two operating points ($\Phi = 0.36$ and $\Phi = 0.18$); the device—designed for harsh environments—has been characterized for sensitivity, linearity, and hysteresis, ensuring suitability for high-frequency pressure-induced vibrations. The analysis integrates raw time traces, PDFs/kurtosis, FFT/PSD, Cross-FFT with POD modes, SPOD, and band-limited ACF to (i) separate persistent tonal behavior from intermittent lean-near-blowout dynamics, and (ii) map sensor content onto coherent flame modes, thereby clarifying the added value of compact, robust, CMOS-compatible accelerometry for instability detection under realistic conditions [35,36].

Consequently, the structure of the present work is organized as follows. Section 2 describes the experimental details: specifically, Section 2.1 is devoted to the fabrication and functional characterization of the piezoelectric accelerometer, while Section 2.2 presents the experimental set-up for combustion monitoring. Section 3 reports the results and the related discussion, divided into subsections. Section 3.1 illustrates the preliminary characterization of the accelerometer, whereas Section 3.2 analyzes the sensor performance under realistic combustion operating conditions. Within this section, Section 3.2.1 focuses on the visualization of flame regimes; Section 3.2.2 analyzes the temporal correlation between the signals acquired from the piezo-MEMS accelerometer and the commercial pressure sensor, including a statistical characterization of combustion instabilities through probability density functions (PDFs), kurtosis, and frequency-domain analysis via FFT. Section 3.2.3, on the other hand, focuses on the spectral and spatial characterization of the instabilities, using Cross-FFT between the acquired signals and the temporal coefficients of the first POD modes, with the aim of identifying the most relevant frequency bands to be further investigated via SPOD for a spatial description of the involved regions. To complete the analysis, the Autocorrelation Function (ACF) is also applied to study oscillatory behavior, and wavelet decomposition is used to provide a time–frequency representation of the instabilities. Finally, Section 4 summarizes the main conclusions of the work.

This study is, to the best of our knowledge, the first to demonstrate the application of a monolithically integrated uniaxial piezoelectric MEMS accelerometer to monitor instability patterns induced by fuel–air modulation (Jet-A1 with air addition) within a combustor environment. The integration of this MEMS device represents a significant advancement toward the development of compact, cost-effective, and scalable sensor solutions for real-time combustion diagnostics.

2. Experimental details

2.1. Fabrication and functional characterization of the piezoelectric accelerometer

The device was fabricated in the cleanroom of CNR-IMM following the process depicted in Fig. 1. Starting from Silicon-on-insulator (SOI) substrate, consisting of a single crystalline silicon top layer (device layer 10 μm-thick) separated from the handle wafer (400 μm-thick) by a thin buried layer (1 μm-thick) of a thermal silicon oxide (SiO_2), Ti bottom electrode 150 nm-thick was sputtered after lithography step (a). A second photolithography outlines the area where AlN thin film 500 nm-thick is deposited by sputtering (b). Subsequently, Ti top electrode is deposited on AlN layer and silicon device layer is deep etched by Inductive Couple Plasma (ICP) down to silicon oxide etch stop layer (c). The front side of the wafer is protected by a 3.5 μm thick, hard baked polymeric film (photoresist) to proceed with the back pattern process which involves the deep etching of silicon proof mass by ICP and the wet etching of silicon oxide in BOE (Buffered oxide etchant) (d). After the etching of 400 μm Si handle layer, the suspended structures are released (e).

The photo in Fig. 1f shows the fabricated piezoelectric accelerometer after the chips separation. The circular simmetry guarantees a preferred displacement along the axis perpendicular to the plane of the proof-mass, reducing the contribution coming from the other two axes [37].

2.2. Test set-up for combustion monitoring

An experimental investigation took place at the Green Engine laboratory of the University of Salento. The test bench, consisting of a 300-kW liquid-fueled swirled combustor, includes a cylindrical combustion chamber with an internal diameter of 4 cm and a length of 29 cm. A schematic drawing is shown in Fig. 2.

An external compression system, equipped with a resistive preheater, provides the overall airflow, which is introduced into the combustion chamber through two separate flows via concentric annular tubes.

The inner tube incorporates an eight-blade axial swirler with a vane exit angle of 45°. The corresponding swirl number is $S\sim0.8$, which falls in the typical range for axial swirlers in gas-turbine combustors ($S\sim0.5 - 1.2$) and is commonly classified as moderate swirler [38]. At $S\sim0.8$ the flow leaving the swirler carries a substantial tangential momentum relative to the axial component, promoting rapid fuel–air mixing and flame stabilization via a sustained central recirculation zone. The combustion chamber is also equipped with a closed-loop water cooling system, driven by an electric pump, which ensures thermal control of the entire structure during operation. The Jet-A1 is pumped at 7 bar with a Pierburg 7.21659.72.0 pump and sprayed into the combustion chamber through a single-hole nozzle (Steinen 1.35 45° S), with an injection angle of 45°. The primary airflow constitutes 91.5 % of the total airflow, while the remaining enters axially into the combustion chamber. The fuel mass flow rate was measured with the VSE EF 0.04 ARO 14 V PNP/2 flow meter, with an accuracy of ±2 % of the reading. The air mass flow rate was estimated by measuring the volumetric flow rate under standard conditions with the Asa-C6-3100/38/EX1 flow meter (accuracy: ±1 % f.s.v.) [39].

Regarding the diagnostic equipment, the combustion chamber

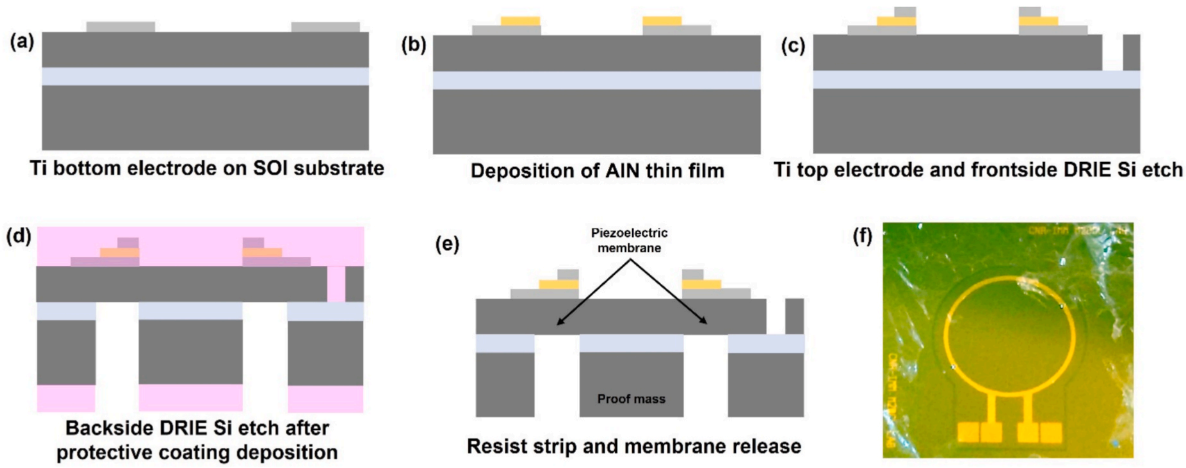

Fig. 1. Flowchart of the process steps followed for the fabrication of the MEMS piezoelectric accelerometer; in (f) the accelerometer after the separation of single chips (10 x 10 mm^2die area).

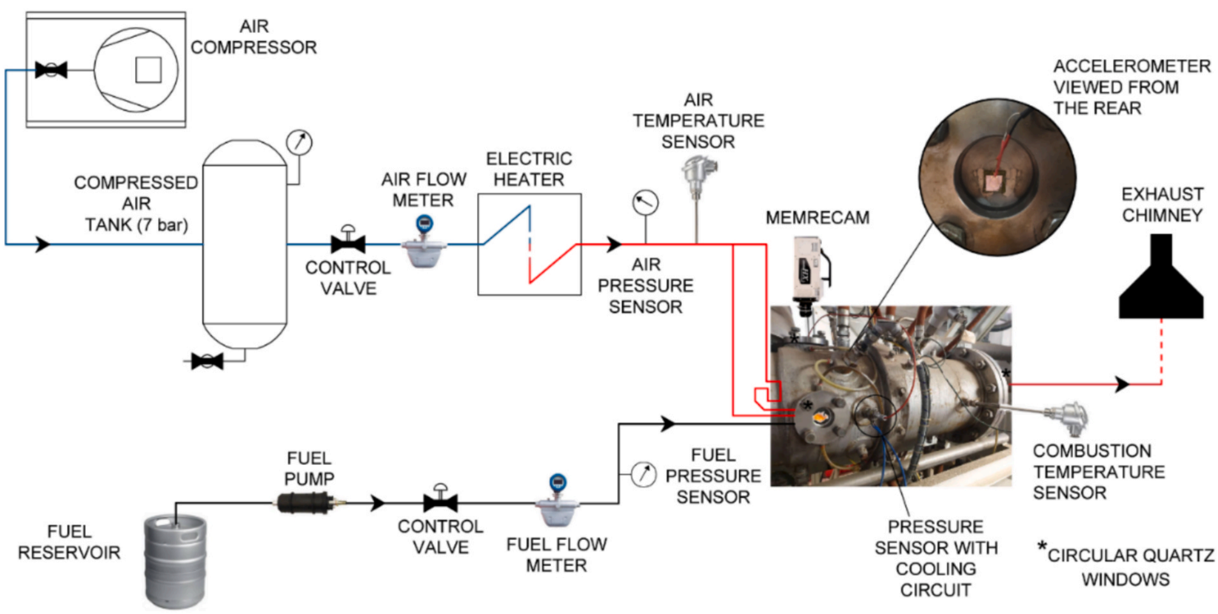

Fig. 2. Green Engine combustion chamber set-up diagram.

pressure was monitored with a Kistler PiezoSmart Type 4045A2 pressure sensor (piezoresistive type), placed near the flame in the combustion zone. This sensor was connected to a piezoresistive amplifier Type 4618A0, with a pressure range of 0–2 bar. The pressure sensor was integrated into a cooling circuit, ensuring forced coolant circulation through a dedicated pump to keep the local temperature below the maximum operating limit of 413 K.

The microfabricated piezoelectric accelerometer was positioned on the combustion chamber structure near the flame in the combustion zone, on the opposite side of the pressure sensor (Fig. 2). This position was chosen to maximize the sensor response towards combustion process signals, minimizing the contribution coming from other noise sources and guarantee comparable acoustic propagation paths for both sensors. Moreover, the wall temperature in the vicinity of the sensor never exceeded ~673 K, thanks to the combustion chamber design and its integrated cooling system. Although no specific thermal protection was implemented for the device, the active piezoelectric material (AlN) had been previously tested up to ~723 K, demonstrating high structural and functional stability. Throughout the entire experimental campaign, no significant variations or signal degradations attributable to thermal effects were observed.

Pressure and accelerometric data were acquired at a sampling frequency of 10 kHz using a National Instruments LabVIEW control and acquisition system. The presence of optical access to the combustion chamber allowed for the acquisition of images of the combustion process. The combustor is equipped with three circular quartz windows: one with a perpendicular-lateral axis with respect to the combustor axis, a second with a perpendicular-upward axis, and a third in the axial direction, as illustrated in Fig. 2. The circular window with a perpendicular-upward axis was used to mount a Memrecam GX-1F camera by NAC Image Technology for image visualization. For each test condition, 1000 images were captured at a frequency of 1000 Hz. Each image captured by the Memrecam had a resolution of 1280 × 1024 pixels and, after cropping, the field of view was approximately 45 × 56 mm. Various statistical, spectral and wavelet-based methods have been developed to establish correlations between the extracted parameters and the physical properties that characterize unstable flames. The distribution for the second moment (variance) and the kurtosis could help in the study of time signals. With these parameters it is possible to have a quantitative indicator of the instability [40]. The fundamental frequencies of combustion were obtained from the pressure and accelerometer signals under investigation by means of FFT techniques and wavelet decomposition. Finally, flame characteristics were extracted from the images through temporal observation of the phenomenon. Visible structures can highlight areas of chemical activity or regions of significant fluctuations in heat release. Table 1 summarizes the applications of each data analysis technique.

For the characterization of the microfabricated piezo-MEMS accelerometer in working conditions, experimental tests of self-induced instability were conducted using Jet-A1 fuel. Preheated inlet air at a temperature of 410 K was used, controlling the air mass flow rate at 40 g/s and 80 g/s respectively, while keeping the fuel mass flow rate constant at 1.00 g/s. This resulted in two different equivalence ratios (Φ) close to the Lean Blowout (LBO), specifically 0.36 and 0.18, determined as follows:

$$\Phi = \left(\frac{\dot{m}_f}{\dot{m}_a}\right)/\left(\frac{\dot{m}_f}{\dot{m}_a}\right)_{st} \tag{2}$$

where $\dot{m}$ represents the mass flow rate and the subscripts f and a indicate the fuel and air flows, respectively, while st denotes stoichiometric conditions with a stoichiometric fuel/air ratio of 14.5. The operating pressure inside the combustion chamber was kept at atmospheric level (1 bar).

The distribution of fuel and air within the combustor is not spatially uniform; therefore, the equivalence ratio should be understood as the global fuel/air ratio.

3. Results and discussion

3.1. Preliminary characterization of the accelerometer

Before testing the device in working conditions, bench experiments were performed, aimed to evaluate the resonance frequency, the quality factor, and the linearity of the microfabricated accelerometer. The signal were acquired along the perpendicular of the proof-mass plane. The resonance frequency is identified by studying the frequency response of the device, as shown in Fig. 3. It has been investigated by sweeping the frequency of the shaker in the range of 100 Hz to 5000 Hz and applying an acceleration equal to 1 g. A maximum of the output voltage is recorded at 3800 Hz, resulting the resonance frequency of the accelerometer. Amplitude-frequency characteristic curve is of great importance because it allows to determine the working frequency range, too. As observable from Fig. 3, the curve is relatively smooth up to 1200 Hz that results the working frequency band of the sensor. From the amplitude – frequency characteristic curve, the quality factor Q of the accelerometer can be calculated. It is given by the following formula:

$$Q = \frac{f_{res}}{\Delta f_{0.5V}} \tag{1}$$

where f_{res} is the resonance frequency and $\Delta f_{0.5V}$ is the bandwidth at half the peak voltage after the Lorentzian fitting of the curve shown in the inset of Fig. 3. Q-factor is equal to 12.3 with the fitting R-squared value of 0.98. The output voltage of the accelerometer was recorded at different acceleration g in the range 0.5 – 0.8 g, at fixed frequency of 500 Hz, to evaluate the sensitivity of the sensor. Fig. 4 depicts the linear fitting of the voltage versus acceleration, providing a sensitivity equal to 0.25 mV/g.

Hysteresis behaviour of the device has been investigated too, by recording the output voltage of the accelerometer, according to g travel (increasing or decreasing). The acceleration g range is 0.5 – 0.8 g. Both travels have been plotted in Fig. 5. As observable, they match almost well indicating that the device keeps a satisfying linearity.

3.2. Multi-domain analysis and MEMS–pressure correlation under lean combustion conditions

For the characterization of the microfabricated piezo-MEMS accelerometer under operating conditions, experimental tests of self-induced instability were conducted using Jet-A1 fuel. The experimental conditions adopted are described in Section 2.2.

The acquired data were analysed in three complementary stages, presented in the subsequent subsections. In Section 3.2.1, a preliminary investigation of the instantaneous flame dynamics was conducted for both test cases (Φ = 0.36 and Φ = 0.18), using high-speed visualizations of broadband chemiluminescence. Section 3.2.2 presents the statistical characterization of combustion instabilities based on time-domain metrics—namely, mean, variance, and kurtosis—followed by spectral

Table 1
Summary of the applications of each data analysis technique.

Data analysis technique	Dataset	Purpose
Instantaneous Time Series	Luminance Images	To improve understanding of flame instability through the brightness of images that evolve over time
Dynamic Correlation	Pressure Signals Accelerometer Signals	Determine how pressure and acceleration signals are closely related.
Variance and Kurtosis	Pressure Signals Accelerometer Signals	To quantify the stability of a combustion process
Fast Fourier Transform	Pressure Signals Accelerometer Signals	To identify dominant frequency components and their contributions to the signals
Cross-Fast Fourier Transform	Luminance Images Pressure Signals Accelerometer Signals	To analyze how the FFTs of the eigenvalues extracted from the POD are correlated with the accelerometer or with the pressure signals
Spectral Proper Orthogonal Decomposition	Luminance Images	To study the combustion structures within the frequency ranges identified through the Cross-FFT
Autocorrelation Function	Luminance Images	To analyze periodicity, temporal coherence, and regularity in oscillatory signals through the temporal coefficients of the frequency ranges obtained from SPOD
Wavelet Decomposition	Pressure Signals Accelerometer Signals	To analyze the signals at different scales and capture transient phenomena

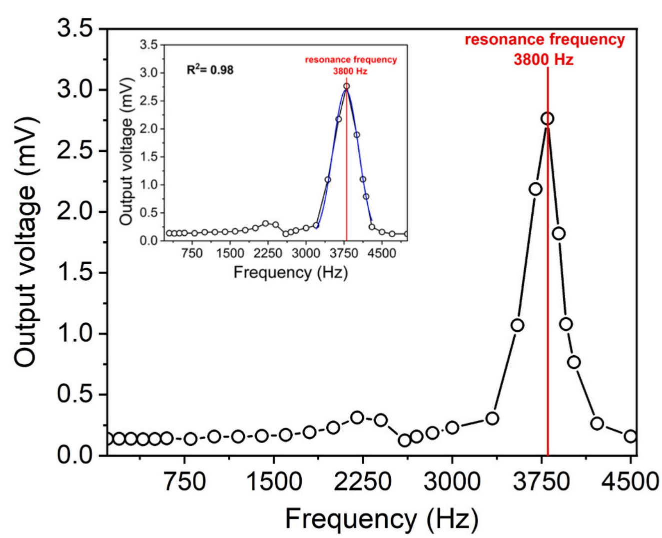

Fig. 3. Frequency response evaluated in the frequency range from 100 Hz to 5000 Hz at @1g; the resulting resonance frequency is equal to 3800 Hz with a working frequency range up to 1200 Hz. In the inset the Lorentzian fitting to obtain the parameters for Q calculation.

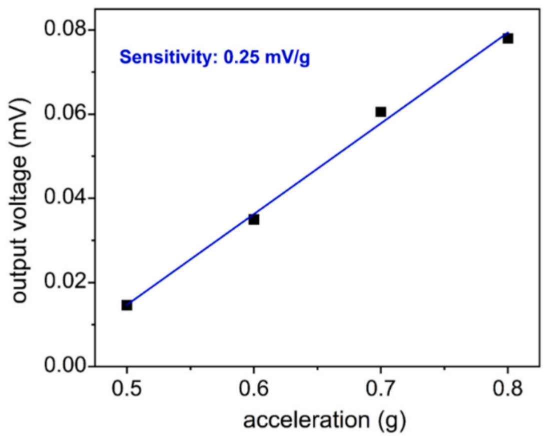

Fig. 4. Voltage sensitivity of the accelerometer obtained from the slope of the linear fitting of the experimental data recorded at the frequency of 500 Hz.

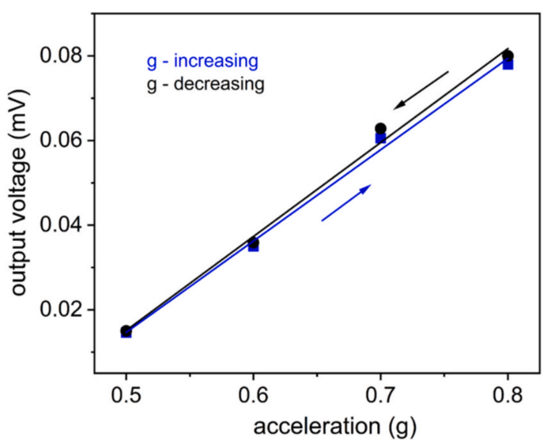

Fig. 5. Hysteresis behaviour of the DUT by considering increasing and decreasing acceleration values in the range 0.5–0.8 g.

analysis via FFT. Finally, in Section 3.2.3 focuses on the spectral and spatial characterization of the instabilities, using Cross-FFT with the coefficients of the first POD modes to identify the most relevant frequency bands for further analysis via SPOD. The analysis is complemented by the ACF to study oscillatory behaviour and by wavelet decomposition to provide a time–frequency representation of the instabilities.

3.2.1. Visualisation of flame regimes

To support the characterization of combustion regimes and evaluate the performance of the piezo-MEMS accelerometer under lean and potentially unstable conditions, high-speed optical imaging was employed to capture the spatiotemporal evolution of the flame. This qualitative analysis serves as a visual reference for interpreting the dynamic features detected by pressure and vibration sensors, enabling a clearer understanding of regime transitions, oscillatory behaviour, and spatial asymmetries typically associated with thermoacoustic instabilities.

Compared with pressure-only diagnostics, these images expose spatial asymmetries and intermittency that inform the interpretation of sensor signals, enabling a more defensible distinction between phase-locked tonal behaviour ($\Phi = 0.36$) and intermittent, blowout-driven dynamics ($\Phi = 0.18$).

The flame visualization complements sensor-based diagnostics by providing insight into flame stability, geometry, and propagation patterns—key parameters for identifying early signs of instability. The analysis focuses on $\Phi = 0.36$ and $\Phi = 0.18$, both close to the Lean Blowout (LBO) limit, in order to contrast stable and unstable combustion regimes under well-controlled experimental conditions [41].

Fig. 6 presents a time sequence of flame evolution at $\Phi = 0.36$, captured using the Memrecam GX-1F high-speed camera.

The images were captured through a circular quartz window using a high-speed camera (Memrecam GX-1F), with a temporal resolution of $\Delta t_1 \sim 0.1$ s. The sequence consists of ten consecutive frames, spanning a total observation period of 1 s (from $t_0 + \Delta t_1$ to $t_0 + 10\Delta t_1$). The injector nozzle is highlighted in red, and the flame is observed along both axial and radial directions (dimensions in mm).

The grayscale intensity indicates flame luminance and serves as a qualitative proxy for local heat release and combustion activity. In the initial frames, the flame appears compact and well-defined near the injector, with low brightness levels—indicative of limited combustion intensity. As time progresses, the flame expands upward, and increased luminance—particularly in the central region—suggests enhanced heat release and the onset of more active combustion. Although the flame remains moderately symmetric, the intensity distribution is non-uniform.

Toward the later frames, a broadening of the upper flame region becomes evident, indicating enhanced turbulent mixing and lateral spreading. Brighter zones likely correspond to areas of higher thermal energy or luminous emissions caused by incandescent particles or intensified reaction zones. This dynamic behaviour is characteristic of lean premixed combustion, which typically exhibits more irregular and less cohesive flame structures compared to richer mixtures.

To deepen the comparative analysis of combustion regimes, Fig. 7 presents the flame behavior at $\Phi = 0.18$. As in the previous case, ten time-resolved frames were acquired using the high-speed camera with a temporal resolution of $\Delta t_2 \sim 0.1$ s. The flame is observed through the same circular quartz window (white border), with the injector nozzle marked in red.

At this highly lean condition, the flame appears significantly weaker than in the $\Phi = 0.36$ case. The grayscale intensity remains generally low across all frames. Bright regions are localized, sparse, and irregular in shape, suggesting intermittent combustion activity and non-uniform flame propagation.

In the early frames, the flame structure is fragmented and exhibits poor spatial cohesion. Unlike the more stable and upward-expanding flame observed at $\Phi = 0.36$, this flame shows limited radial and axial development. Notably, several frames (e.g., $t_0 + 3\Delta t_2$, $t_0 + 5\Delta t_2$, $t_0 + 10\Delta t_2$) reveal slender, filament-like luminous structures—indicative of turbulent flame “tongues” that propagate chaotically and rapidly dissipate. These features are characteristic of instability and the proximity to blowout.

In the final frames, the flame becomes increasingly diffuse, with diminished intensity and broader dark zones, especially near the center and upper part of the window. This visual evidence supports the presence of low combustion efficiency, reduced thermal release, and increased susceptibility to flame extinction.

A comparative analysis of Fig. 6 and Fig. 7 highlights the substantial influence of the equivalence ratio on flame structure and stability. At $\Phi = 0.36$, the flame exhibits higher luminance and a more homogeneous intensity distribution along the axial direction, indicative of a stable and energetically sustained combustion process. The flame expands radially in a symmetric and orderly manner, maintaining a compact and well-defined shape throughout the sequence.

Conversely, at $\Phi = 0.18$, the flame appears significantly dimmer and more fragmented, with irregular luminous structures and reduced spatial coherence. The combustion is clearly less efficient, with lower heat release and increased susceptibility to instability or extinction. The presence of intermittent and asymmetric “tongues” of flame suggests turbulent and chaotic propagation dynamics, especially in the upper region of the flame front.

From a morphological perspective, the $\Phi = 0.36$ flame demonstrates

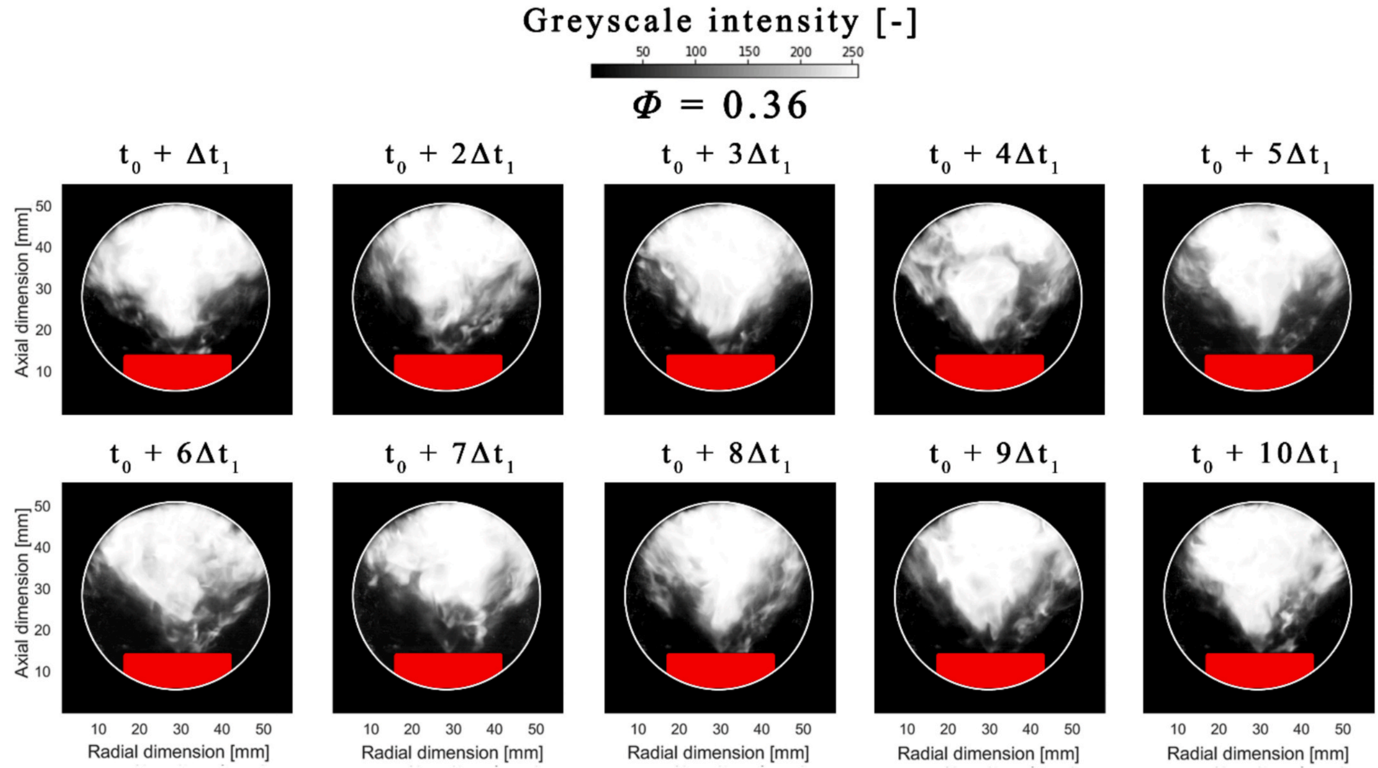

Fig. 6. Visualization through circular quartz window of the instantaneous flame dynamics at various temporal instants for $\Phi = 0.36$; in red the position of the injector nozzle; t0 = 0 s; $\Delta t_1 \sim 0.1$ s. (For interpretation of the references to color in this figure legend, the reader is referred to the Web version of this article).

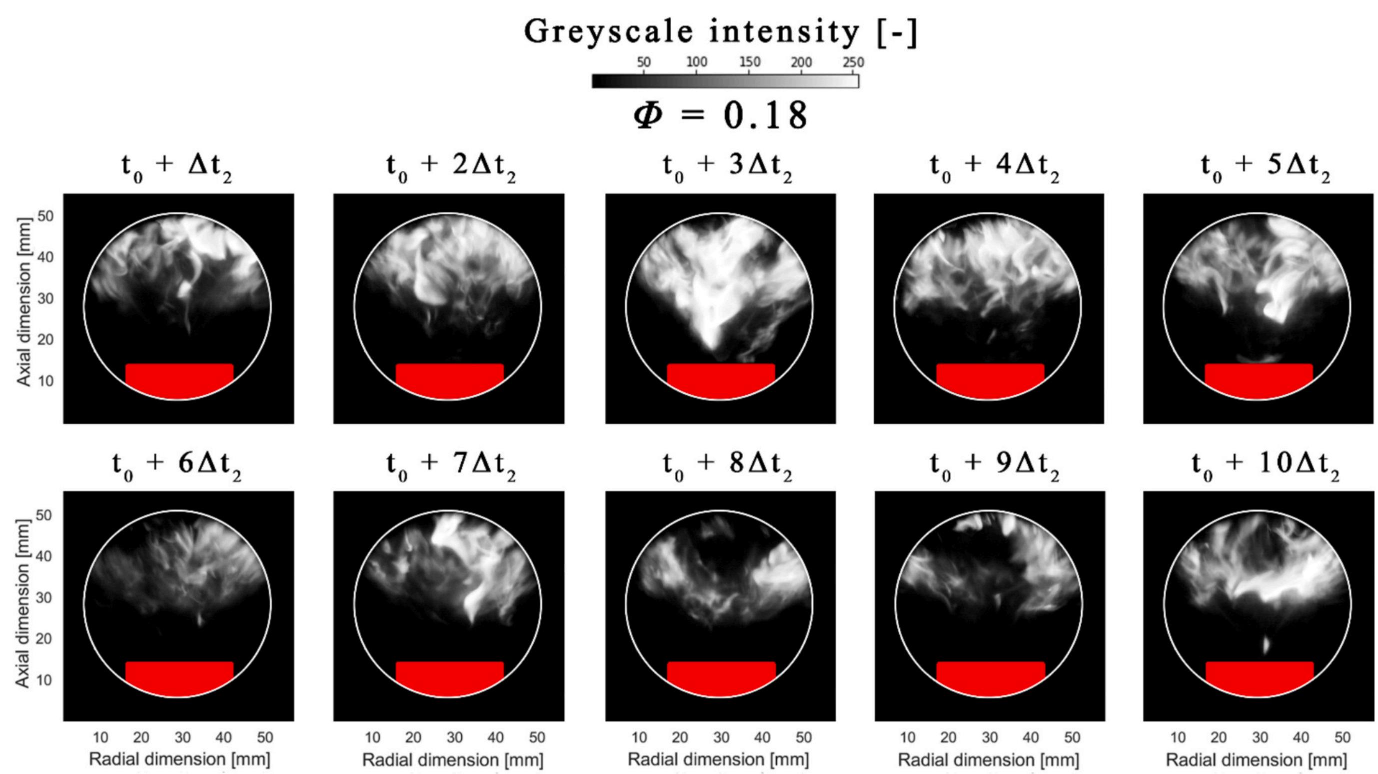

Fig. 7. Visualization through circular quartz window of the instantaneous flame dynamics at various temporal instants for $\Phi = 0.18$; in red the position of the injector nozzle; t0 = 0 s; $\Delta t_2 \sim 0.1$ s. (For interpretation of the references to color in this figure legend, the reader is referred to the Web version of this article).

consistent spatial growth and structural cohesion, while the $\Phi = 0.18$ flame is marked by diffuse contours, erratic expansion, and localized bursts of activity—typical features of a system operating near the lean blowout limit.

3.2.2. Correlation and statistical characterization of combustion instabilities through time- and frequency-domain signals from piezo-MEMS accelerometer and pressure sensor

To evaluate the ability of the microfabricated piezoelectric MEMS accelerometer to reproduce combustion-related dynamic behavior, this subsection analyzes the correlation between its time-domain response and that of a reference commercial pressure sensor. The analysis includes a detailed statistical characterization of the acquired signals and the application of the FFT, which enables the decomposition of the temporal signals into their frequency components.

The analysis was conducted for both test cases at $\Phi = 0.36$ and $\Phi = 0.18$—previously characterized through optical diagnostics and statistical analysis. Both signals were acquired at a sampling rate of 10 kHz to capture high-frequency fluctuations linked to combustion instabilities and mechanical vibrations.

Fig. 8 reports the time-domain signals acquired by the piezo-MEMS accelerometer (top) and the commercial pressure sensor (bottom). The figure highlights the ability of the piezo-MEMS device to reliably detect the dynamic fluctuations associated with combustion, showing consistent behavior with the reference pressure sensor and accurately reproducing the main temporal features of the pressure field. Regarding the operating conditions, at $\Phi = 0.18$ the air–fuel mixture is very lean: the reaction time increases and the flame becomes more sensitive to velocity and pressure perturbations, thereby promoting thermoacoustic coupling and the onset of instability, even close to blow-off. Conversely, at $\Phi = 0.36$ the richer mixture results in a more stable and robust flame, less prone to self-excited oscillations and capable of acoustically damping pressure fluctuations.

Fig. 9 displays the evolution of the Pearson correlation coefficient between the two signals over time, offering insight into the degree of coherence between pressure-induced combustion dynamics and structural vibrations captured by the accelerometer.

The fluctuations in the graph indicate that the relationship between pressure and acceleration dynamically varies typically between −1 and 1. A value of 1 or −1 indicates perfect positive or negative correlation, respectively, while a value of 0 indicates no correlation [42,43,44]. To highlight the temporal evolution of the Dynamic Correlation Coefficient, a smoothed trend line (in red) was superimposed on the raw data (in blue). The trend was obtained using a moving average filter, which effectively reduces high-frequency fluctuations while preserving the overall behavior of the signal. The window length for the moving average was selected to ensure an optimal balance between noise suppression and temporal resolution, allowing for a clearer interpretation of the underlying correlation dynamics.

The dynamic correlation between the time signals of the chamber pressure and the piezo-MEMS accelerometer remains consistently high for both operating conditions ($\Phi = 0.36$ and $\Phi = 0.18$), with correlation coefficients in the range 0.9964–0.9982. The high values indicates that the MEMS accelerometer coherently tracks combustion-driven pressure fluctuations, confirming its suitability for real-time monitoring without physical access to the chamber.

A slightly larger temporal variability of the correlation at $\Phi = 0.18$ is evident, which is consistent with intermittent lean-near-blowout behaviour observed in flame imaging and time-series statistics (broader PDFs and higher kurtosis).

Despite the fundamental difference in physical quantities—pressure sensors measuring in-chamber thermodynamic variations and accelerometers responding to structural vibrations—the high and stable correlation highlights the MEMS device's reliability. These results reinforce the piezo-MEMS accelerometer's potential as a compact, CMOS-compatible solution for real-time combustion diagnostics, even under

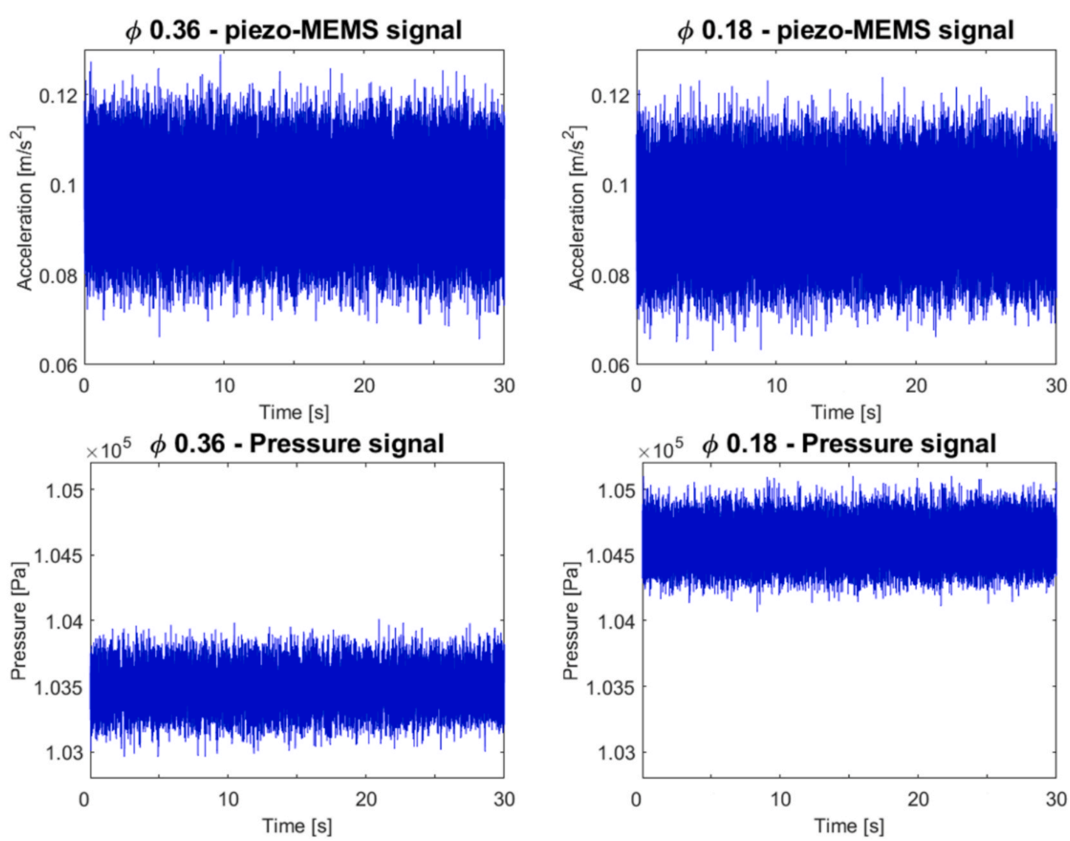

Fig. 8. Time-domain comparison between the piezo-MEMS accelerometer (top) and the chamber pressure fluctuation (bottom).

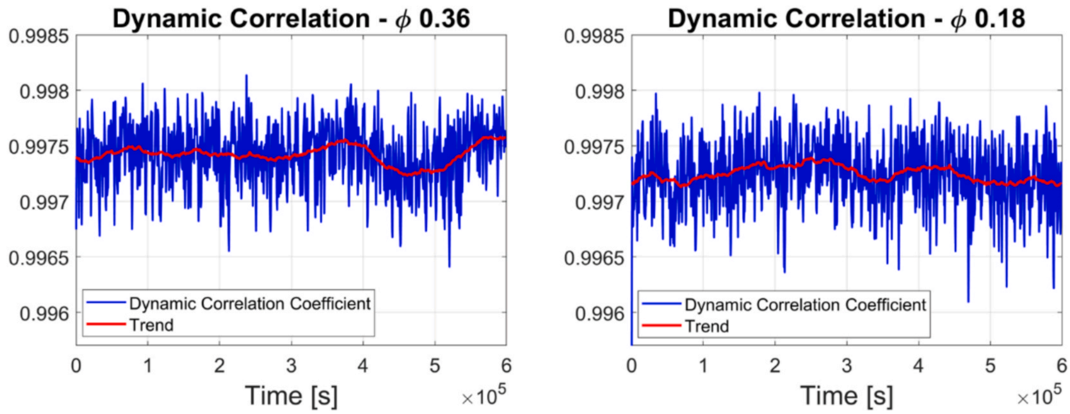

Fig. 9. Dynamic correlation between the time signals of the commercial pressure sensor and the microfabricated piezo-MEMS accelerometer for both test cases.

highly unsteady operating conditions and without the need to physical access to combustion chamber.

To gain deeper insights into combustion dynamics under varying equivalence ratios, a detailed statistical analysis is carried out on the temporal signals acquired from both the microfabricated piezo-MEMS accelerometer and the commercial pressure sensor. These signals are evaluated under two test conditions ($\Phi = 0.36$ and $\Phi = 0.18$), previously analyzed through optical diagnostics and correlation assessments.

Statistical descriptors such as mean, variance, and kurtosis provide quantitative insight into the amplitude and distribution of signal fluctuations, serving as indicators of combustion stability. Moreover, signal processing techniques including the FFT and Wavelet Energy decomposition are employed to identify dominant frequency components and transient phenomena. These methods collectively support the detection of irregular combustion behavior and the early identification of instability onset. Practical applications of these techniques include monitoring and diagnosing flame instabilities in internal combustion engines and gas turbines. Through statistical analysis and Fourier transform, early warning signals of combustion issues can be identified, while Wavelet Energy provides a detailed view of temporal fluctuations [45,46,47].

Fig. 10 shows the probability density functions (PDFs) of the time signals acquired from the accelerometer (left) and the pressure sensor (right) for both test conditions, normalized to 1 to allow a direct comparison of the distribution shapes and spreads, independent of differences in mean values. The figure clearly shows that, for $\Phi = 0.18$, the distributions are broader and flatter compared to those observed at $\Phi = 0.36$, indicating a higher degree of signal variability. This effect is particularly evident in the accelerometer signal, which exhibits greater deviation compared to the sharper distribution in the $\Phi = 0.36$ case. These broader distributions are consistent with increased turbulence, combustion irregularity, and flame instability, as confirmed by flame visualizations (Fig. 6 and Fig. 7) and the analysis of raw signals (Fig. 8). Despite the regime-dependent differences, the distributions remain approximately Gaussian in all four cases, indicating that the systems remain within statistically stable bounds, without signs of multimodality or strong skewness. These results confirm that leaner mixtures ($\Phi = 0.18$) exhibit higher signal dispersion and less predictable dynamics,

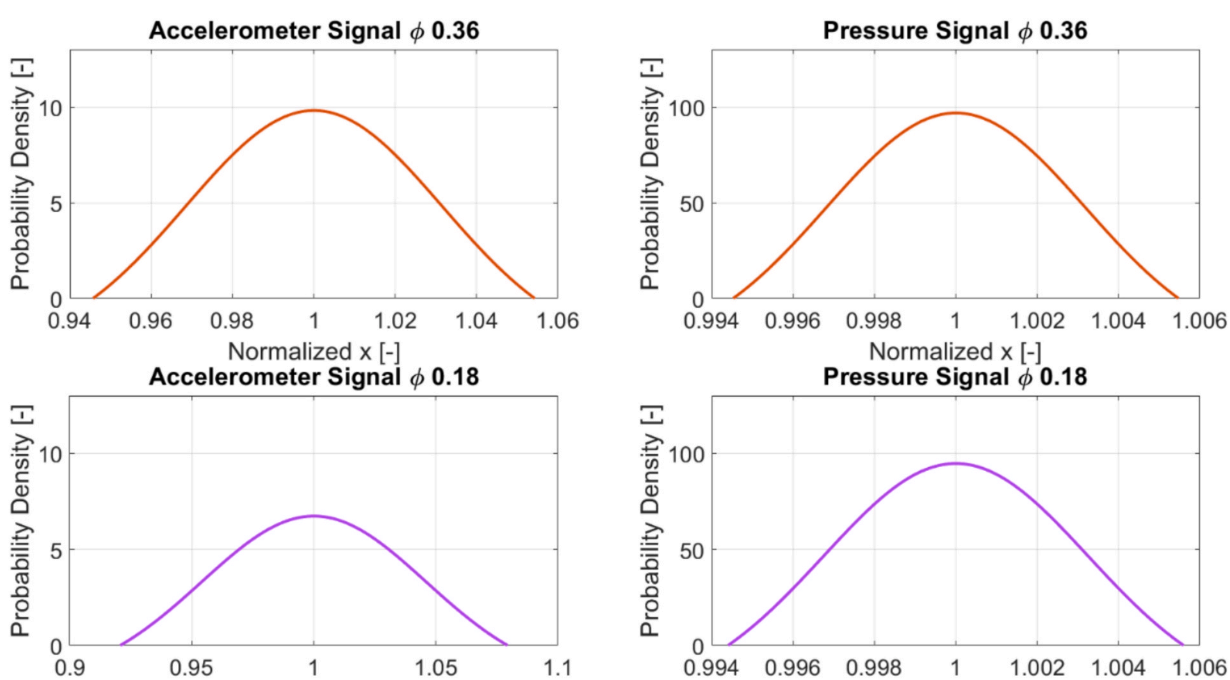

Fig. 10. Trend of the variance normalized to 1 on a probability density scale for the time signals of the commercial pressure sensor and the microfabricated piezo-MEMS accelerometer for both test cases.

whereas the richer condition ($\Phi = 0.36$) promotes greater stability, reflected in narrower and more peaked distributions. The accelerometer proves particularly sensitive to these regime changes, making it an effective tool for non-intrusive combustion diagnostics.

This trend is quantitatively confirmed by the kurtosis values reported in Table 2. Kurtosis values are close to the Gaussian reference (3) in all cases, yet a systematic increase appears at the leaner condition ($\Phi = 0.18$), most clearly in the accelerometer (3.3420 vs 3.0587) and, to a lesser extent, in pressure (3.0651 vs 3.0146). In this study, instability is defined operationally as a departure from stationary, narrowband behavior, evidenced by greater intermittency and dynamic variability in the signals. Within this definition, an increase in kurtosis indicates heavier tails—i.e., more frequent high-amplitude excursions—consistent with intermittent events in a lean, near-blowout regime. Interpreted together with the broader full-band PDFs, the larger time-domain dispersion, the less prominent dominant line in the spectra, and the faster decay of SPOD-based autocorrelation, the kurtosis rise at $\Phi = 0.18$ supports classification of this operating point as more intermittent and less stationary rather than a phase-locked limit cycle. Kurtosis is thus used as one element of an integrated criterion, and its modest but consistent increase across sensors aligns with independent diagnostics.

These statistical features reinforce earlier observations that leaner combustion ($\Phi = 0.18$) leads to less predictable and more chaotic flame dynamics, which are effectively captured by both pressure and vibration-based measurements [48].

The higher kurtosis values previously observed for $\Phi = 0.18$ suggest the presence of intermittent high-energy events potentially linked to flame instability and resonance. To gain a clearer understanding of the system's dynamic response, a FFT was performed on the signals acquired from both the piezo-MEMS accelerometer and the commercial pressure sensor.

In contrast to single-metric approaches, the joint use of PDFs, kurtosis, and raw time traces provides convergent evidence of intermittency at $\Phi = 0.18$ while maintaining sensor agreement; this multi-indicator view improves interpretability over pressure-only or accelerometer-only baselines.

The FFT plays a complementary role by decomposing the time signals into their frequency components, helping to identify dominant oscillatory modes and instability signatures. While the pressure sensor reflects direct thermodynamic fluctuations, the accelerometer captures structural responses to combustion-induced forces. Together, their frequency spectra—analyzed via FFT—enable real-time monitoring of instabilities and potential early detection of critical combustion events [49,50,51].

As shown in Fig. 11, the resulting spectra provides valuable insight into the dominant frequency components and the dynamic response of the combustion system under different equivalence ratios. In the accelerometer signal for $\Phi = 0.36$, the spectrum is characterized by a smooth decay, with most of the spectral energy concentrated below 1000 Hz. A prominent peak is observed around 200 Hz (FFT amplitude ~0.35), likely associated with structural vibration modes of the combustor. For $\Phi = 0.18$, the accelerometer spectrum maintains a similar shape but with reduced amplitude (peak ~0.27–0.30), reflecting lower vibrational intensity due to less coherent combustion, as also observed in the flame imaging and statistical signal analysis.

On the pressure signal side, the FFT for $\Phi = 0.36$ reveals a dominant low-frequency peak, likely associated with primary acoustic or thermoacoustic modes, and some isolated higher-frequency components. For $\Phi = 0.18$, these peaks become more pronounced, with higher amplitude and additional sharp resonances, indicating a stronger pressure oscillatory response and potential excitation of combustion chamber resonant modes. The pressure signal for $\Phi = 0.36$ shows a strong low-frequency peak near 250 Hz (amplitude 0.065), along with isolated minor peaks at higher frequencies (2900 Hz and ~3400 Hz), possibly indicating weak resonance phenomena. In contrast, the $\Phi = 0.18$ pressure signal displays a more pronounced low-frequency peak (250 Hz, amplitude ~0.14) and stronger high-frequency components, with visible peaks at approximately 3000 Hz and 3500 Hz. This spectral broadening reflects amplified pressure oscillations and suggests the presence of combustion instabilities or excitation of higher-order acoustic modes in lean conditions.

These spectral features confirm that leaner operation ($\Phi = 0.18$) amplifies both pressure oscillations and signal variability, reinforcing its association with unsteady and less efficient combustion regimes. The spectral differences between the two equivalence ratios confirm that leaner mixtures ($\Phi = 0.18$) introduce greater combustion variability and pressure pulsation intensity, which can lead to more turbulent and less predictable dynamic behavior. The MEMS accelerometer proves capable of capturing these changes, albeit with less frequency selectivity compared to the pressure sensor. The criteria adopted to assess combustion stability are therefore not based solely on the global shape of the PDF (which remains approximately Gaussian in both cases), but on an integrated analysis of dispersion, kurtosis, and frequency spectra. Taken together, these indicators demonstrate that the lean mixture ($\Phi = 0.18$) is associated with a more unstable and less predictable behavior, whereas the richer condition ($\Phi = 0.36$) ensures greater stability and signal regularity.

Table 2
Kurtosis values for the two test cases and for both sensors.

Φ	Kurtosis	
	Accelerometer	Pressure sensor
0.36	3.0587	3.0146
0.18	3.3420	3.0651

3.2.3. Spectral and spatial characterization of combustion instabilities through Cross-FFT, SPOD and ACF

To identify spectral components shared among the signals (acceleration, pressure) and the POD modal time coefficients, a cross-spectral analysis (hereafter "Cross-FFT") was performed with identical windowing and segmentation across datasets. In this study, Cross-FFT is used solely to localize frequencies that are jointly active, highlighting energy alignment in the frequency domain. A normalized coherence measure was not computed; accordingly, results are not to be interpreted as a 0–1 "degree of coherence," but rather as indicators of shared bands subsequently examined with SPOD.

The Cross-FFT was restricted to 0–500 Hz, the range most relevant for comparison with POD-based image decomposition and consistent with the Nyquist limit of the high-speed image sequences. SPOD was then applied to bands below 100 Hz, where principal structural and pressure fluctuations concentrate, and the ACF was used to characterize the time persistence of coherent structures within those bands [52]. The Cross-FFT allows for identifying shared frequency components and determining whether such components are in-phase or out-of-phase, revealing the level of correlation at different frequencies. The Cross-FFT is computed by multiplying the FFT of one signal by the complex conjugate of the FFT of the second signal, according to the formula:

$$Y_{cross}(f) = Y_{signal1}(f) \bullet Y^{*}_{signal2}(f) \quad (3)$$

In this expression, $Y_{cross}(f)$ represents the Cross-FFT, $Y_{signal1}(f)$ is the Fourier Transform of the first signal, and $Y^{*}_{signal2}(f)$ is the complex conjugate of the transform of the second signal. This product highlights the interaction and correlation between the frequencies present in the two analyzed signals. The amplitude of the Cross-FFT provides a measure of the correlation intensity for each frequency, enabling the identification of spectral components that are common to both signals. If the amplitude is high for a particular frequency, it indicates that this frequency is shared and that there is a strong relationship between the two signals in that frequency band [53].

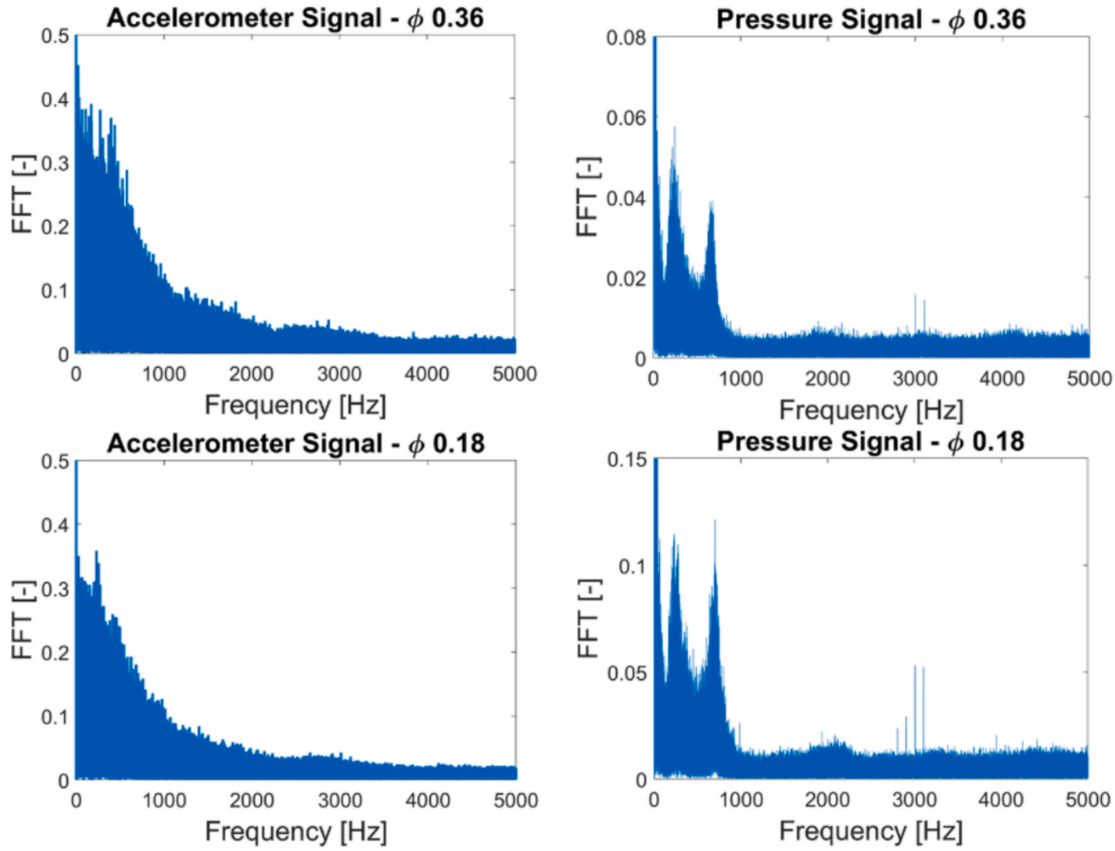

Fig. 11. Fast Fourier Transform of the commercial pressure sensor and the microfabricated piezo-MEMS accelerometer for both test cases.

The POD method decomposes flow fields into orthogonal spatial modes associated with temporal coefficients, ranking them by their energy contribution (eigenvalues). This technique enables the identification of coherent flame structures and their dominant frequencies. The resulting eigenmodes represent the most energetically significant oscillations in the flame field.

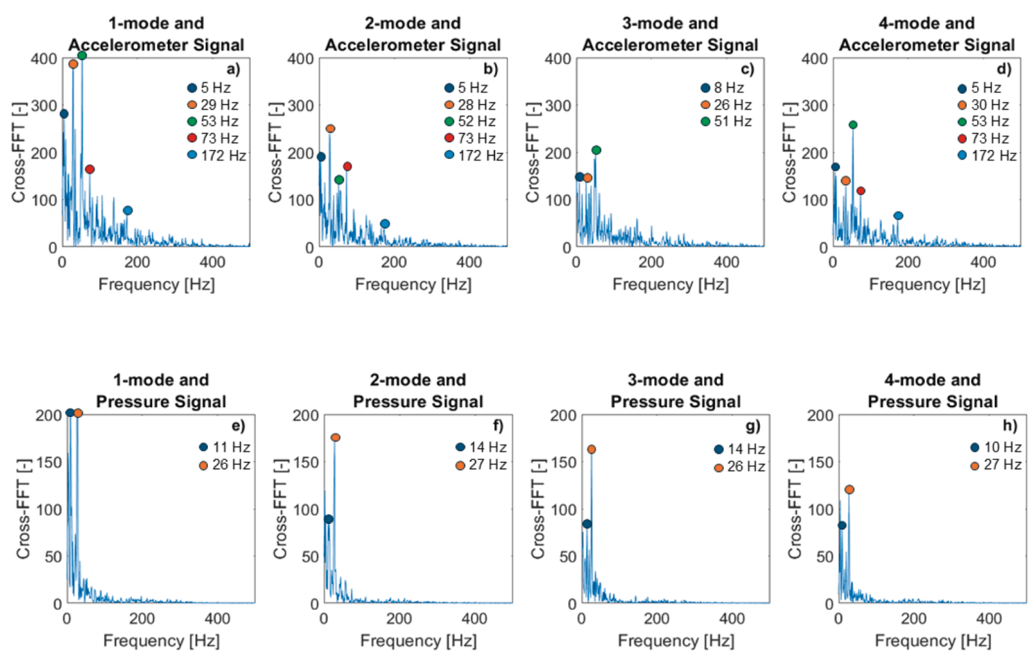

Figure 12: Cross-Fast Fourier Transform of Φ = 0.36 between the main POD modes and the accelerometer (a-d) and the pressure signal (e-h).

Fig. 12. Cross-Fast Fourier Transform of $\Phi = 0.36$ between the main POD modes and the accelerometer (a-d) and the pressure signal (e-h).

The cross-FFT analysis shown in Fig. 12 highlights a significant correlation between the FFT of the first four modes extracted through the POD eigenvalue decomposition, the FFT of the accelerometer signal, and the FFT of the pressure signal, with a global equivalence ratio of 0.36.

To highlight this, the values of the frequencies that are repeated for multiple modes were shown. The POD technique is used to characterize the behavior of flames through a space–time analysis of acquired images. It extracts an orthogonal basis of eigenvalues from flow data, separating spatial and temporal contributions to identify coherent modal structures in the system. The eigenvalues, calculated from data correlation, quantify the energy associated with different modes, providing an indication of the relative importance of each modal structure. For further details on the POD technique, the authors refer to another of their paper [38].

Considering the graphs a-d, the correlation is stronger for the lower-order modes, with predominant peaks at low frequencies, indicating a greater interaction with the system's oscillations. In fact, the frequencies that recur across multiple modes are below 73 Hz, with an exception for a peak at 172 Hz. Higher-order modes exhibit weaker spectral contributions, suggesting a lesser influence on the accelerometer signal and indicating that the dynamics represented by these modes have a reduced global impact. Regarding the cross-FFT analysis between the first four modes obtained from the POD and the pressure signal, only two correlation peaks are observed at frequencies of 12 ± 2 Hz and 26 ± 1 Hz. The first modes (e-f), compared to the subsequent ones (g-h), suggest a greater relevance in describing the dynamic interaction between the system and the pressure signal.

Overall, the cross-spectral coupling is stronger and more widely distributed in the accelerometer than in the pressure signal, likely because the accelerometer captures both local mechanical responses and flow-induced vibrations, whereas the pressure sensor responds more selectively to global thermodynamic fluctuations.

These findings confirm that the relevant frequencies driving both structural vibration and pressure fluctuations are mainly concentrated below 200 Hz, and that modal energy is concentrated in the first few POD modes. The identification of shared frequency components provides valuable information on how flame dynamics couple with sensor-detectable oscillations.

To further isolate the coherent structures underlying the observed frequency-domain features, SPOD is applied. Unlike classical POD, SPOD operates directly in the frequency domain, allowing the decomposition of flow fields into orthogonal spatial modes ranked by spectral energy. This approach enables the identification of dominant structures at specific frequencies, making it particularly effective for analyzing statistically stationary but dynamically complex flows [54]. SPOD provides a concise and physically meaningful representation of the main energetic modes and their spectral distribution. For further details on its theoretical formulation and implementation, see [30].

The SPOD analysis was focused mainly on frequencies below 100 Hz, since the preliminary Cross-FFT results showed that the dominant frequencies, governing both structural vibrations and pressure fluctuations, are concentrated in this spectral region. Therefore, based on the dominant frequency peaks identified in the cross-FFT analysis (Fig. 12), Fig. 13 to Fig. 17 present the spatial visualization of the first four SPOD modes, extracted from high-speed, broadband flame images at $\Phi = 0.36$, covering three frequency bands: [0–15.63] Hz, [15.63–31.25] Hz, and [46.88–62.5] Hz. Each mode is associated with a specific energy λ, indicating its relative importance within the frequency range. The modal energy values (λ) quantitatively indicate the contribution of each mode to the overall flow energy, while the normalized amplitude fields reveal the spatial distribution and intensity of oscillatory behavior. The visualizations highlight how the energy is concentrated in different spatial regions across frequency bands, unveiling the underlying mechanisms that drive flame instabilities and coherent motion in the reacting flow.

In the lowest band (Fig. 13), the SPOD modes show large-scale coherent structures with high energy, especially Mode 1 ($\lambda = 34$) and Mode 2 ($\lambda = 15$), which correspond to strong Cross-FFT peaks in the 5–30 Hz range. Mode 2 displays a symmetric double-lobe shape aligned with the injector axis, characteristic of radial oscillations, while Mode 4 ($\lambda = 4.7$) exhibits more fragmented and localized features, suggesting weaker coherence. In the mid-frequency band (Fig. 14), the structures become more complex and asymmetric. Mode 1 ($\lambda = 110$) is the most energetic overall, revealing off-axis vortical behavior possibly related to convective instabilities, and Modes 2–4 ($\lambda = 58, 36, 22$) show growing irregularity, aligning with Cross-FFT peaks around 26–29 Hz. In the higher-frequency range (Fig. 15), the SPOD modes appear more localized and fragmented, with Mode 1 ($\lambda = 45$) clearly capturing jet-like activity near the nozzle, likely linked to shear-layer dynamics or injection effects. Modes 2–4 ($\lambda = 25, 23, 13$) reflect spatial decoupling and chaotic motion, in agreement with weaker but still observable Cross-FFT peaks at 50–53 Hz.

The trend continues in Fig. 16 ([62.5–78.13 Hz]), where Mode 1 ($\lambda = 32$) retains some coherent organization, but Modes 2–4 ($\lambda = 15, 13, 8.9$) show highly variable, asymmetric features, consistent with the diminishing dominance of organized modes at increasing frequency. Finally, in the highest analyzed band ([171.88–187.5 Hz], Fig. 17), modal energy is significantly reduced ($\lambda = 5$ to 3.2), and all four modes exhibit weakly structured, noisy spatial fields with no dominant directionality—signatures of residual uncorrelated or weakly coupled fluctuations. This progressive transition from highly coherent, energetic structures at low frequencies to disorganized, low-energy modes at high frequencies confirms the frequency-localized nature of flame dynamics under $\Phi = 0.36$. The comparison across all frequency bands supports the

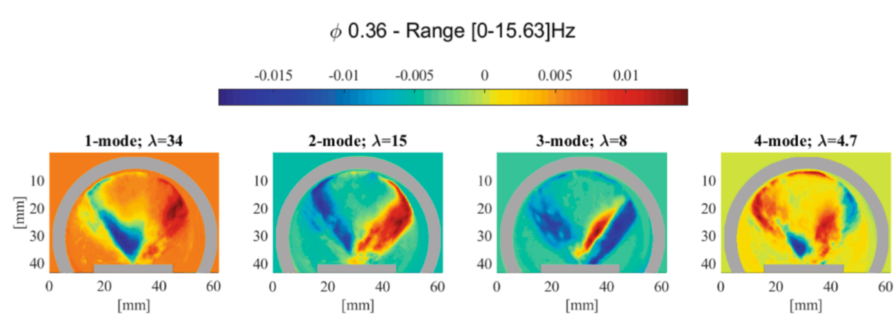

Figure 13: SPOD modes 1–4 of the broadband images at Φ = 0.36 acquired through the high-speed MemreCAM camera for range [0-15.63]Hz. The grey circular arc outlines the optical circular window, while the grey rectangle indicates the nozzle position. (For interpretation of the references to color in this figure legend, the reader is referred to the Web version of this article).

Fig. 13. SPOD modes 1–4 of the broadband images at $\Phi = 0.36$ acquired through the high-speed MemreCAM camera for range [0–15.63]Hz. The grey circular arc outlines the optical circular window, while the grey rectangle indicates the nozzle position. (For interpretation of the references to color in this figure legend, the reader is referred to the Web version of this article).

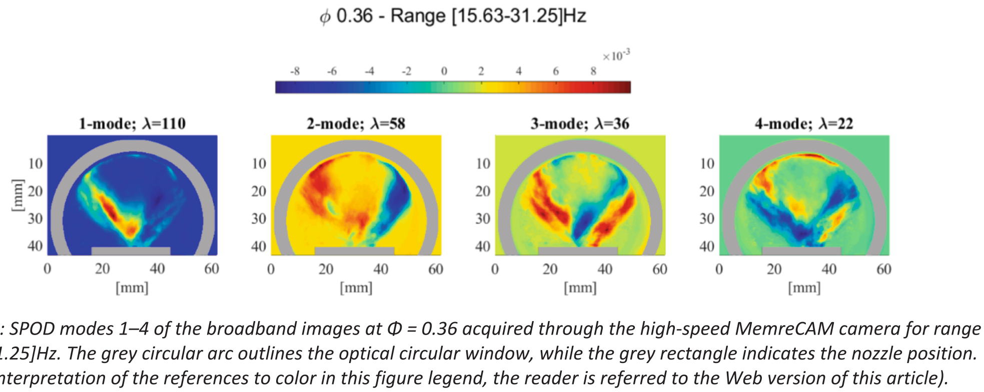

Fig. 14. SPOD modes 1–4 of the broadband images at $\Phi = 0.36$ acquired through the high-speed MemreCAM camera for range [15.63–31.25]Hz. The grey circular arc outlines the optical circular window, while the grey rectangle indicates the nozzle position. (For interpretation of the references to color in this figure legend, the reader is referred to the Web version of this article).

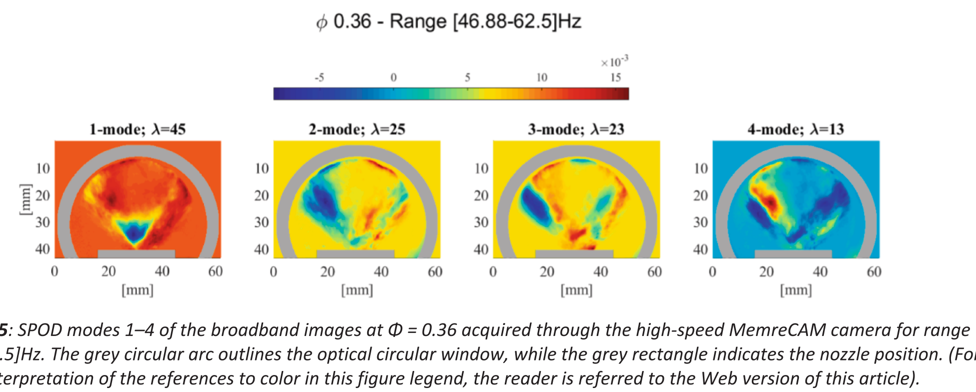

Fig. 15. SPOD modes 1–4 of the broadband images at $\Phi = 0.36$ acquired through the high-speed MemreCAM camera for range [46.88–62.5]Hz. The grey circular arc outlines the optical circular window, while the grey rectangle indicates the nozzle position. (For interpretation of the references to color in this figure legend, the reader is referred to the Web version of this article).

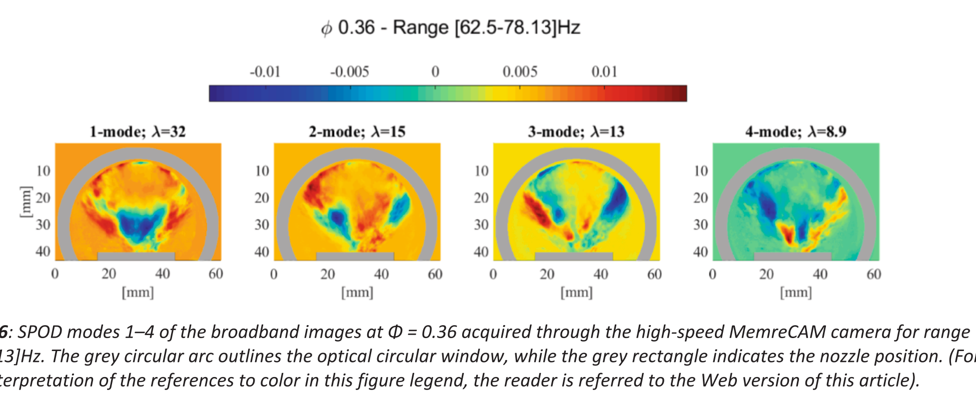

Fig. 16. SPOD modes 1–4 of the broadband images at $\Phi = 0.36$ acquired through the high-speed MemreCAM camera for range [62.5–78.13]Hz. The grey circular arc outlines the optical circular window, while the grey rectangle indicates the nozzle position. (For interpretation of the references to color in this figure legend, the reader is referred to the Web version of this article).

interpretation that dominant instabilities reside in the 0–75 Hz range, while higher frequencies represent minor contributions or unresolved turbulent activity. The close agreement between SPOD-extracted spatial modes and Cross-FFT peaks validates the combined use of frequency-domain decomposition and sensor correlation techniques to characterize coherent combustion structures and their dynamic coupling to measurable physical quantities.

The ACF is a valuable tool for assessing the temporal persistence and potential periodicity of signals, as it measures the correlation of a signal with itself as a function of time lag. For a more theoretical discussion, the reader is referred to another work by the same authors [38]. Fig. 18 reports the normalized ACF of the SPOD modal time coefficients for $\Phi = 0.36$. In the low-frequency bands (0–15.6 and 15.6–31.3 Hz) the ACF shows regular peaks with a gradually decaying envelope, indicating coherent low-frequency modulation of the flame/flow field. Moving to the intermediate bands (46.9–62.5 and 62.5–78.1 Hz), the ACF decays faster and oscillations become less persistent, consistent with more localized or transient dynamics. In contrast, the high band near the

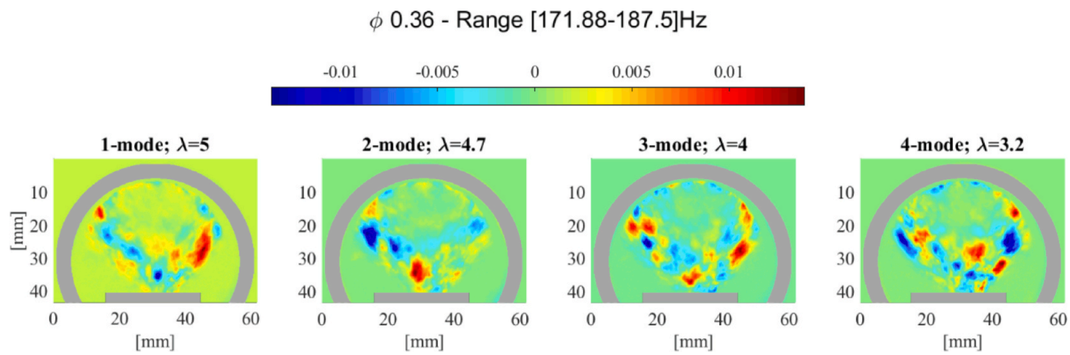

Fig. 17. SPOD modes 1–4 of the broadband images at $\Phi = 0.36$ acquired through the high-speed MemreCAM camera for range [171.88–187.5]Hz. The grey circular arc outlines the optical circular window, while the grey rectangle indicates the nozzle position. (For interpretation of the references to color in this figure legend, the reader is referred to the Web version of this article).

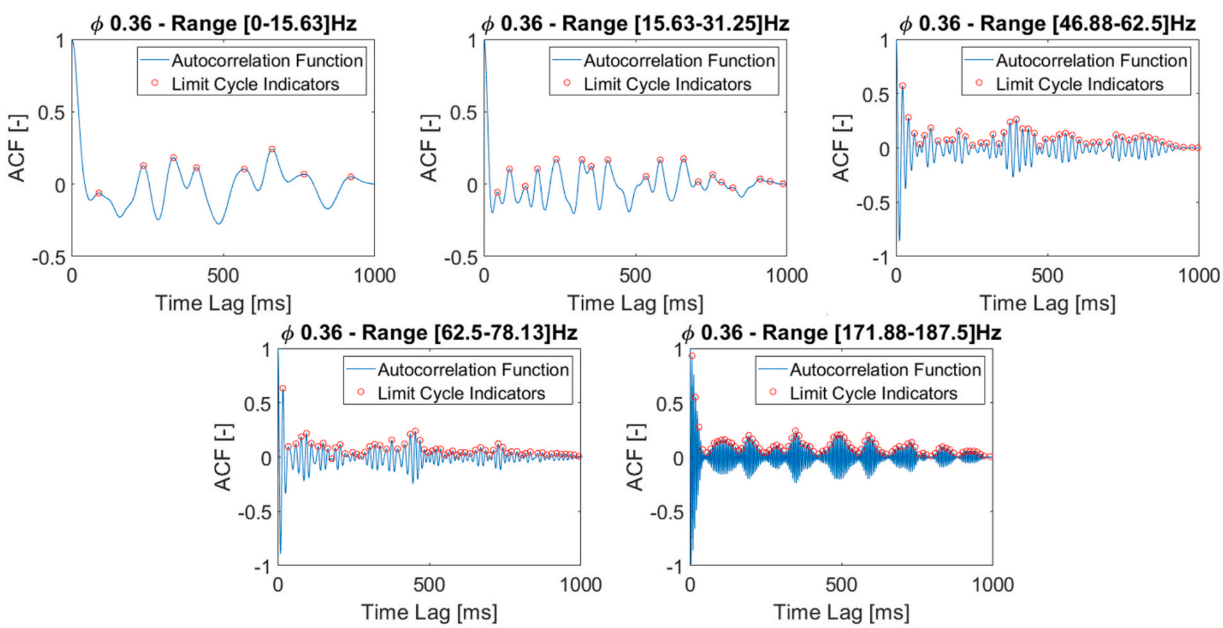

Fig. 18. Autocorrelation function for the $\Phi = 0.36$ case, corresponding to the frequency ranges identified through SPOD.

acoustic tone (171.9–187.5 Hz) exhibits the clearest quasi-periodic signature, with regular, long-lived ACF oscillations at lags close to the band period—evidence of a persistent tonal component in the $\Phi = 0.36$ case. Taken together, the band-limited ACFs complement the SPOD spectra by linking time-domain persistence to the dominant spatial structures identified at each frequency range.

The cross-spectral maps localize shared frequency bands, and SPOD/ACF link them to coherent spatial structures and their temporal persistence. This fusion of sensors with POD/SPOD goes beyond prior studies by mapping measurable signals onto flame modes, clarifying which structures couple to pressure versus acceleration.

Fig. 19 presents the Cross-FFT analysis between the first four POD modes and the time signals from the piezoelectric MEMS accelerometer (a–d) and the commercial pressure sensor (e–h) at $\Phi = 0.18$. Compared to the richer condition ($\Phi = 0.36$), the amplitudes of the cross-spectral peaks are generally lower, especially in the pressure signal plots, indicating a weaker spectral coupling between the dominant POD modes and the pressure signal. This suggests that under ultra-lean conditions, the flame dynamics are less energetically coupled to global pressure oscillations, possibly due to incomplete or intermittent combustion.

In the accelerometer-based Cross-FFT (a–d), several pronounced peaks are still present, particularly in the low-frequency range (0–100 Hz), confirming that this band remains the most relevant for vibrational response. Frequencies that appear consistently across multiple modes include 5 Hz, 13 Hz, 20 Hz, 28 Hz, 38 Hz, and up to 176 Hz, with Modes 2 and 4 showing broader spectral content. These repeated frequencies indicate a persistence of structured oscillations and localized interactions between flame dynamics and structural vibration, even in the presence of instability.

By contrast, the pressure signal correlations (e–h) exhibit fewer and less intense peaks, mostly concentrated below 65 Hz. Recurring components are visible at 5–6 Hz, 12–14 Hz, 28–29 Hz, and 64 Hz, suggesting that pressure fluctuations under lean conditions are dominated by a limited number of low-frequency modes with reduced spatial coherence. The attenuated coupling further confirms that pressure dynamics are less sensitive to high-frequency flow features, while the accelerometer continues to capture finer modal interactions.

As done for the case $\Phi = 0.36$, the corresponding SPOD modes for $\Phi = 0.18$ are also spatially visualized based on the frequency peaks identified in Fig. 19. The energies λ and the color bars are relative to the 4 modes of each frequency range. The dynamics for this global equivalence ratio differ from the previous case, as instability phenomena occur and the motions exhibit translational behavior.

The SPOD analysis for $\Phi = 0.18$, shown in Fig. 20 through Fig. 24, reveals the evolution of coherent structures as a function of frequency and highlights the increasingly fragmented and unstable flame dynamics

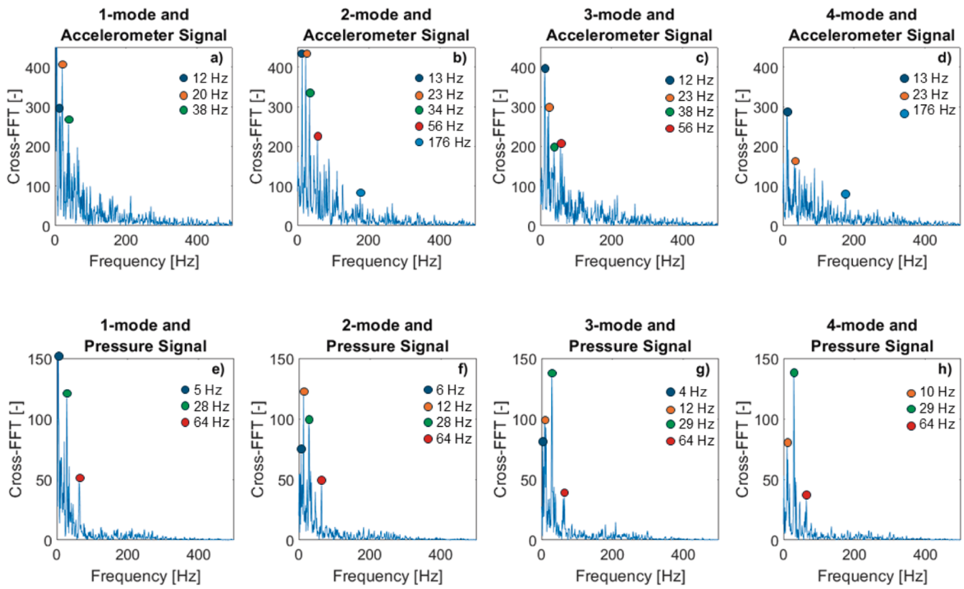

***Figure 19**: Cross-Fast Fourier Transform of Φ = 0.18 between the main POD modes and the accelerometer (a-d) and the pressure signal (e-h).*

Fig. 19. Cross-Fast Fourier Transform of $\Phi = 0.18$ between the main POD modes and the accelerometer (a-d) and the pressure signal (e-h).

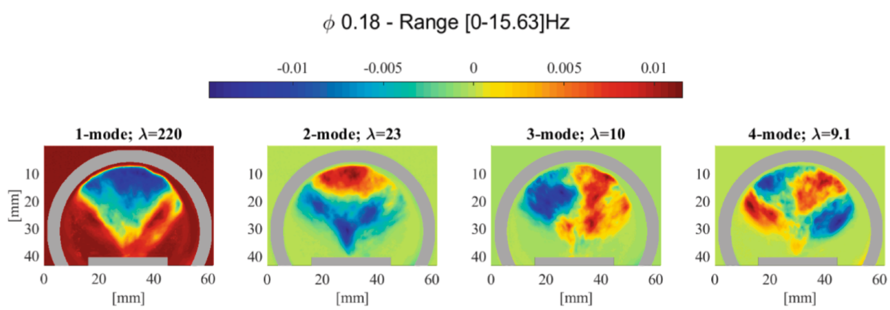

***Figure 20**: SPOD modes 1–4 of the broadband images at Φ = 0.18 acquired through the high-speed MemreCAM camera for range [0-15.63]Hz. The grey circular arc outlines the optical circular window, while the grey rectangle indicates the nozzle position. (For interpretation of the references to color in this figure legend, the reader is referred to the Web version of this article).*

Fig. 20. SPOD modes 1–4 of the broadband images at $\Phi = 0.18$ acquired through the high-speed MemreCAM camera for range [0–15.63]Hz. The grey circular arc outlines the optical circular window, while the grey rectangle indicates the nozzle position. (For interpretation of the references to color in this figure legend, the reader is referred to the Web version of this article).

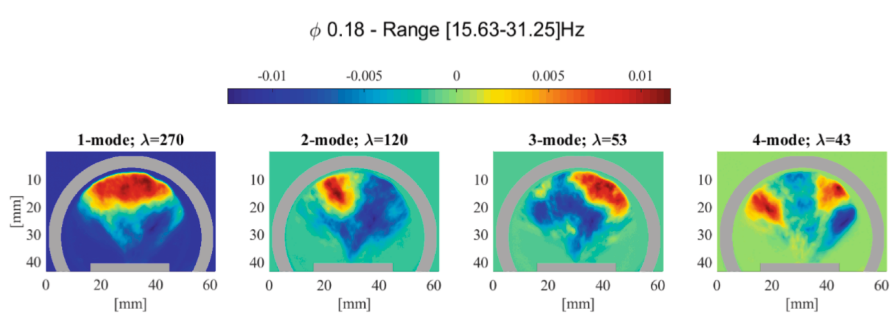

***Figure 21**: SPOD modes 1–4 of the broadband images at Φ = 0.18 acquired through the high-speed MemreCAM camera for range [15.63-31.25]Hz. The grey circular arc outlines the optical circular window, while the grey rectangle indicates the nozzle position. (For interpretation of the references to color in this figure legend, the reader is referred to the Web version of this article).*

Fig. 21. SPOD modes 1–4 of the broadband images at $\Phi = 0.18$ acquired through the high-speed MemreCAM camera for range [15.63–31.25]Hz. The grey circular arc outlines the optical circular window, while the grey rectangle indicates the nozzle position. (For interpretation of the references to color in this figure legend, the reader is referred to the Web version of this article).

under ultra-lean conditions. In the lowest frequency band ([0–15.63 Hz], Fig. 20), Mode 1 ($\lambda = 220$) is characterized by a highly symmetric and intense structure, suggesting a globally organized oscillation, possibly associated with low-frequency acoustic or base flow instabilities. This symmetry progressively breaks down in Modes 2–4 ($\lambda = 23, 10, 9.1$), which exhibit doublet-like shapes and increasingly localized perturbations with fluctuating hot (red) and cold (blue) regions, indicative of incipient chaotic motion and reduced coherence.

As the frequency increases to the [15.63–31.25 Hz] band (Fig. 21), the modal energy remains high—especially for Mode 1 ($\lambda = 270$) and Mode 2 ($\lambda = 120$)—and the spatial structures become more asymmetric, with concentrated intensity around the reaction zone and sharper transitions between high- and low-intensity regions. This suggests the presence of large-scale convective instabilities with strong coupling to the heat release field. The structures are still coherent but begin to exhibit signs of directional bias and lateral oscillations, in agreement with the dominant frequencies observed in the Cross-FFT.

In the next frequency range ([31.25–46.88 Hz], Fig. 22), the SPOD modes show a further shift toward fragmentation. Although Mode 1 ($\lambda = 110$) retains a relatively organized lobe, Modes 2–4 ($\lambda = 72, 62, 39$) reveal complex, multi-lobed features with less consistent orientation, consistent with turbulent deformation of the flame front and flow-field decoupling. These patterns mark a transition zone where turbulent structures begin to dominate over global modes.

Moving into the [46.88–78.13 Hz] band (Fig. 23), modal energy decreases slightly, and spatial complexity increases. Mode 1 ($\lambda = 54$) and Mode 2 ($\lambda = 36$) present intermittent high-intensity spots, while Modes 3 and 4 ($\lambda = 32, 28$) become increasingly patchy, reflecting local turbulence and possibly intermittent shear-layer activity. The absence of large-scale coherence supports the notion that at these frequencies, flow structures are more influenced by stochastic fluctuations than by modal instabilities.

At the highest analyzed range ([171.88–187.5 Hz], Fig. 24), SPOD modes exhibit very low energy ($\lambda = 14$ to 6.5) and highly dispersed structures. Only Mode 1 shows a faint central concentration, while the other modes are dominated by scattered, small-scale oscillations with no clear pattern. These findings indicate that high-frequency content in this ultra-lean regime is associated with residual or background turbulence rather than coherent instabilities. The low modal contribution confirms that such fluctuations play a marginal role in the overall combustion dynamics.

These results are consistent with the Cross-FFT trends, where the dominant coupling between flame structures and sensor signals occurs at low to mid frequencies. Additionally, the progressive loss of spatial coherence and energy content with increasing frequency underscores the fragmented and intermittent nature of combustion at $\Phi = 0.18$.

The SPOD-based autocorrelation analysis, in Fig. 25, ties directly to the lean, near-blowout regime at $\Phi = 0.18$. In the low-frequency bands ($\leq \sim 60$ Hz) the modal time coefficients exhibit rapidly decaying and irregular ACFs, indicative of broadband, intermittent modulation of the heat-release field rather than coherent low-frequency organization. This behaviour is consistent with local extinction/re-ignition and flame–core weakening/detachment expected near blowout in swirl combustors. In the high band around the acoustic tone ($\sim$172–188 Hz), the ACF at $\Phi = 0.18$ shows weaker oscillations and a faster envelope decay than at $\Phi = 0.36$, confirming the absence of a phase-locked limit cycle and the reduced persistence of the tonal component. Taken together with the broader full-band PDFs, higher kurtosis, and the lower tonal contrast in the pressure spectra, the SPOD–ACF results support the classification of $\Phi = 0.18$ as a blowout-driven, intermittently excited regime, in contrast to the more stationary, tone-bearing response observed at $\Phi = 0.36$.

For the ultra-lean case, the reduced cross-spectral coupling in pressure and the fragmented SPOD modes are consistent with blowout-driven intermittency. The accelerometer still captures localized interactions, which helps maintain diagnostic sensitivity where pressure becomes less selectively informative.

To further assess the dynamic instability, wavelet analysis is employed. This enables detection of intermittent oscillations, flame blowoff precursors, and abrupt mode switching by mapping signal energy across time–frequency scales. The combination of SPOD and wavelet analysis thus provides a comprehensive framework for interpreting both spatial and temporal aspects of flame instability in lean regimes. Therefore, the combustion signal is decomposed into a series of Wavelet coefficients that represent the signal's energy in various frequency bands [47,48,49,50,55]. The Fig. 26 shows the Wavelet energy and cumulative energy for the accelerometer and pressure sensor signals for the two test cases ($\Phi = 0.36$ and $\Phi = 0.18$). The signal was decomposed into frequency ranges through eight coefficients, allowing the identification of very low-frequency signals and progressively higher frequency signals. For the accelerometer signal, the Wavelet energy for the test case $\Phi = 0.36$ is always higher than the case $\Phi = 0.18$ except for the 312.5–625 Hz range. The cumulative energy curve for $\Phi = 0.36$ indicates a higher percentage of the total energy, indicating more intense mechanical vibrations typically associated with turbulent combustion.

Conversely, for the pressure signal, the Wavelet energy at low frequencies is significantly higher at $\Phi = 0.18$ compared to $\Phi = 0.36$ up to 2500 Hz. The cumulative curve indicates that at $\Phi = 0.18$, a greater portion of the energy is concentrated in low frequencies, suggesting more prominent pressure fluctuations and possibly more unstable combustion compared to $\Phi = 0.36$. This comparison highlights that different Φ conditions distinctly affect the sensor signals, with $\Phi = 0.36$ resulting in greater vibrational energy and $\Phi = 0.18$ associated with stronger low-frequency pressure fluctuations. Finally, the Wavelet analysis showed that both sensors recorded higher energy content in the 156–312.5 Hz and 312.5–625 Hz frequency ranges.

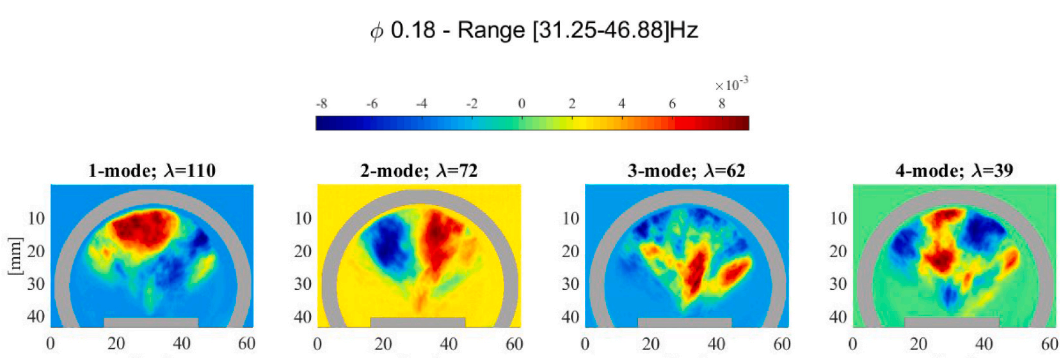

Fig. 22. SPOD modes 1–4 of the broadband images at $\Phi = 0.18$ acquired through the high-speed MemreCAM camera for range [31.25–46.88]Hz. The grey circular arc outlines the optical circular window, while the grey rectangle indicates the nozzle position. (For interpretation of the references to color in this figure legend, the reader is referred to the Web version of this article).

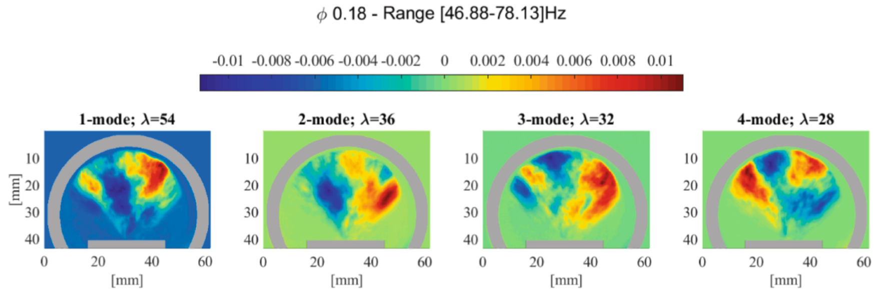

Figure 23: SPOD modes 1–4 of the broadband images at Φ = 0.18 acquired through the high-speed MemreCAM camera for range [46.88-62.5]Hz. The grey circular arc outlines the optical circular window, while the grey rectangle indicates the nozzle position. (For interpretation of the references to color in this figure legend, the reader is referred to the Web version of this article).

Fig. 23. SPOD modes 1–4 of the broadband images at $\Phi = 0.18$ acquired through the high-speed MemreCAM camera for range [46.88–62.5]Hz. The grey circular arc outlines the optical circular window, while the grey rectangle indicates the nozzle position. (For interpretation of the references to color in this figure legend, the reader is referred to the Web version of this article).

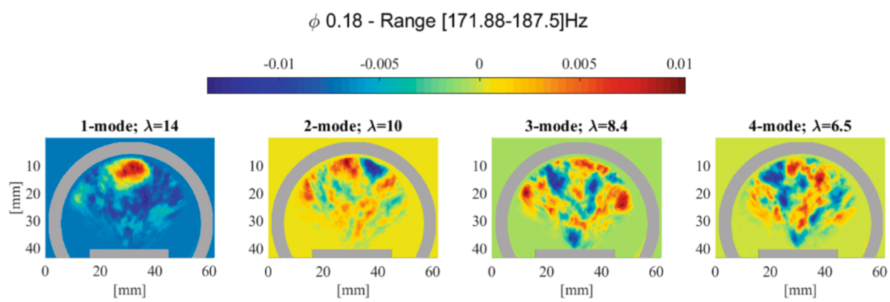

Figure 24: SPOD modes 1–4 of the broadband images at Φ = 0.18 acquired through the high-speed MemreCAM camera for range [171.88-187.5]Hz. The grey circular arc outlines the optical circular window, while the grey rectangle indicates the nozzle position. (For interpretation of the references to color in this figure legend, the reader is referred to the Web version of this article).

Fig. 24. SPOD modes 1–4 of the broadband images at $\Phi = 0.18$ acquired through the high-speed MemreCAM camera for range [171.88–187.5]Hz. The grey circular arc outlines the optical circular window, while the grey rectangle indicates the nozzle position. (For interpretation of the references to color in this figure legend, the reader is referred to the Web version of this article).

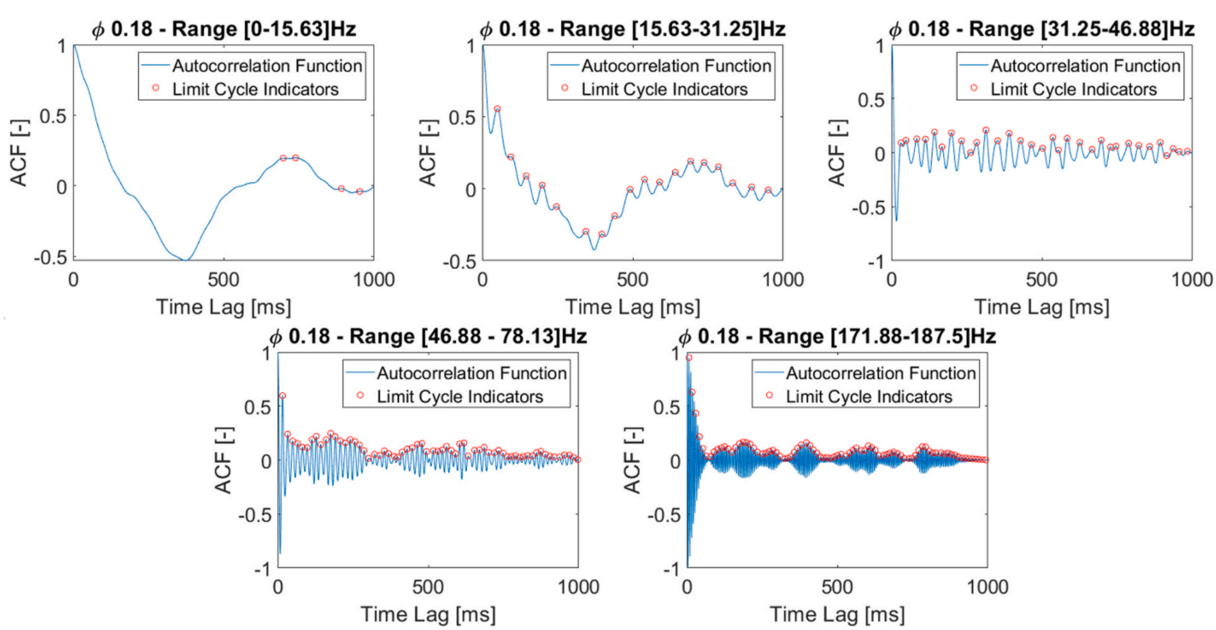

Fig. 25. Autocorrelation function for the $\Phi = 0.18$ case, corresponding to the frequency ranges identified through SPOD.

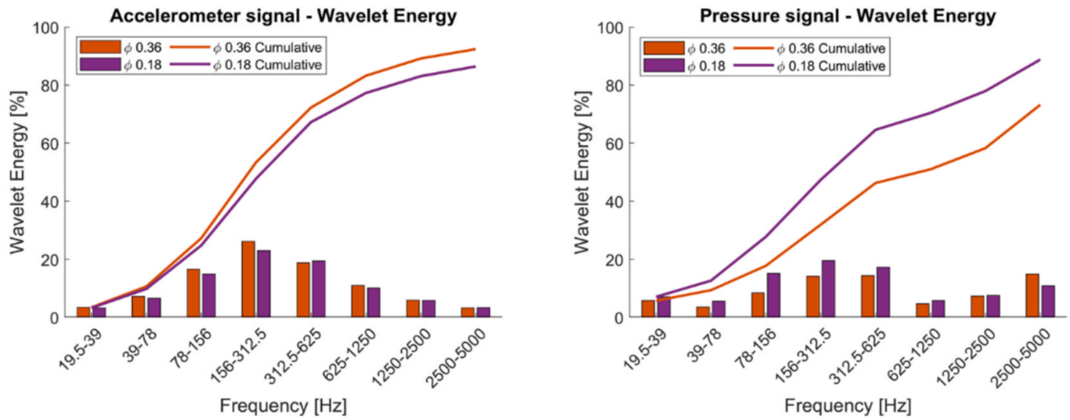

Fig. 26. Wavelet Energy of the pressure sensor and the accelerometer for both test cases.

4. Conclusions

This study characterized combustion dynamics in a swirl-stabilized Jet-A1 combustor at two global equivalence ratios, $\Phi = 0.36$ and $\Phi = 0.18$, using high-speed flame imaging, chamber pressure, and a MEMS accelerometer mounted on the wall. The uniaxial AlN-based piezoelectric MEMS accelerometer, fabricated using standard CMOS-compatible processes, was characterized in terms of sensitivity, linearity, resonance behavior, and hysteresis. Validation under real combustion conditions confirmed its ability to reliably monitor chamber vibrations, with performance directly compared to a commercial pressure sensor.

Flame sequences show a brighter, more cohesive structure at $\Phi = 0.36$ and a dimmer, fragmented, intermittently propagating flame at $\Phi = 0.18$, consistent with operation near lean blowout. Raw time traces confirm that the accelerometer coherently tracks combustion-driven dynamics against pressure; the band-limited, sliding correlation is high in both cases but exhibits greater temporal variability at $\Phi = 0.18$. Full-band PDFs are approximately Gaussian for both conditions yet broader at $\Phi = 0.18$; kurtosis is higher (especially in acceleration), indicating intermittent high-amplitude events. Frequency-domain results show a clearer dominant line near the acoustic mode at $\Phi = 0.36$ and reduced tonal prominence with stronger broadband content at $\Phi = 0.18$ (the same trend appears in acceleration with lower frequency selectivity due to structural filtering and frontend high-pass). Cross-FFT and SPOD link these frequencies to coherent spatial modes: at $\Phi = 0.36$ low-frequency modes are energetic and organized, whereas at $\Phi = 0.18$ modes become fragmented and asymmetric as frequency increases. The band-limited autocorrelation of SPOD modal coefficients indicates longer-lived quasi-periodic content at $\Phi = 0.36$ and faster decorrelation at $\Phi = 0.18$. Wavelet energy further shows higher vibrational energy in acceleration at $\Phi = 0.36$ and higher low-frequency pressure energy at $\Phi = 0.18$. Collectively, these consistent observations validate the AlN MEMS accelerometer as a reliable, compact, non-intrusive, real-time diagnostic, and establish a clear contrast between a tone-bearing regime at $\Phi = 0.36$ and an intermittent, broadband regime at $\Phi = 0.18$.

Considering the harsh environment where the accelerometer works, as the combustion one, the long-term stability of the piezoelectric active film represents a big challenge to face, by investigating new strategies to keep unaltered the piezoelectric response of the nitride (i.e. doping).

CRediT authorship contribution statement

P.Di Gloria: Writing – original draft, Visualization, Methodology, Investigation, Data curation. **M.G.De Giorgi:** Writing – review & editing, Validation, Supervision, Conceptualization. **M.A. Signore:** Writing – original draft, Validation, Supervision, Methodology, Investigation, Data curation, Conceptualization. **L. Francioso:** Writing – original draft, Validation, Supervision, Investigation, Data curation, Conceptualization.

Declaration of competing interest

The authors declare that they have no known competing financial interests or personal relationships that could have appeared to influence the work reported in this paper.

Acknowledgement

The work was supported and funded by the PON R&I 2014–2020 Asse I "Investimenti in Capitale Umano" Azione IV.5 "Dottorati Innovativi sulle tematiche Green" - Corso di Dottorato in "Ingegneria dei Sistemi Complessi" XXXVII ciclo - Università del Salento" and by the PON project SMEA "Tecnologie dei sensori e microsistemi per applicazioni nel settore aeronautico e spaziale" cod. PON03PE_00067_5.

Data availability

Data will be made available on request.

References

[1] Lieuwen T. C., Unsteady Combustor Physics, 2nd ed., Cambridge University Press. 2021, 9781108889001.
[2] Culick, Fred E. C., Paul Kuentzmann, Unsteady Motions in Combustion Chambers for Propulsion Systems, 2006.
[3] Sébastien Candel, Combustion dynamics and control: Progress and challenges, Proceedings of the Combustion Institute, 29(1) (2002) 1–28, ISSN 1540-7489, doi: 10.1016/S1540-7489(02)80007-4.
[4] A. Dowling, A. Morgans, Feedback control of combustion oscillations, Annu. Rev. Fluid Mech. 151–182 (2005), https://doi.org/10.1146/annurev.fluid.36.050802.122038.
[5] Ying Huang, Vigor Yang, Dynamics and stability of lean-premixed swirl-stabilized combustion, Prog. Energy Combust. Sci., 35(4) (2009) 293–364, ISSN 0360-1285, doi: 10.1016/j.pecs.2009.01.002.
[6] C. Paschereit, B. Schuermans, W. Polifke, Mattson, Measurement of transfer matrices and source terms of premixed flames, J. Eng. Gas Turbines Power 239–247 (2002), https://doi.org/10.1115/1.1383255.
[7] A.S. Algamili, M.H.M. Khir, J.O. Dennis, et al., A review of actuation and sensing mechanisms in MEMS-based sensor devices, Nanoscale Res. Lett. 16 (2021) 16, https://doi.org/10.1186/s11671-021-03481-7.
[8] Xianming He, Quan Wen, Zhuang Lu, Zhengguo Shang, Zhiyu Wen, A micro-electromechanical systems based vibration energy harvester with aluminum nitride piezoelectric thin film deposited by pulsed direct-current magnetron sputtering, Appl. Energy 228 (2018) 881–890, ISSN 0306-2619, doi: 10.1016/j.apenergy.2018.07.001.
[9] C. Yang, Hu. Bohao, Lu. Liangyu, Z. Wang, W. Liu, C. Sun, A miniaturized Piezoelectric MEMS accelerometer with polygon topological cantilever structure, Micromachines 13 (10) (2022) 1608, https://doi.org/10.3390/mi13101608.
[10] S. Shi, L. Ma, K. Kang, J. Zhu, Hu. Jinjiang, H. Ma, Y. Pang, Z. Wang, High-sensitivity piezoelectric MEMS accelerometer for vector hydrophones, Micromachines 14 (8) (2023) 1598, https://doi.org/10.3390/mi14081598.
[11] G. Yugandhar, G. Venkateswara Rao, K. Srinivasa Rao, Modeling, Simulation of piezoelectric MEMS sensor, Mater. Today: Proc., 2(4–5) (2015) 1595–1602, ISSN 2214-7853, doi: 10.1016/j.matpr.2015.07.086.

[12] Schuermans, Bruno, Modeling and control of thermoacoustic instabilities. (2003), doi: 10.5075/epfl-thesis-2800.
[13] Camilo F. Silva, Intrinsic thermoacoustic instabilities, Prog. Energy Combust. Sci. 95 (2023) 101065, ISSN 0360-1285, .
[14] L. Barelli, G. Bidini, C. Buratti, R. Mariani, Diagnosis of internal combustion engine through vibration and acoustic pressure non-intrusive measurements, Appl. Therm. Eng., 29(8–9) (2009) 1707–1713, ISSN 1359-4311, doi: 10.1016/j.applthermaleng.2008.07.025.
[15] F. Giuliani, L. Andracher, V. Moosbrugger, N. Paulitsch, A. Hofer, Combined optic-acoustic monitoring of combustion in a gas turbine, Int. J. Turbomach. Propul. Power 5 (3) (2020) 15, https://doi.org/10.3390/ijtpp5030015.
[16] Seongpil Joo, Jongwun Choi, Namkeun Kim, Min Chul Lee, Zero-crossing rate method as an efficient tool for combustion instability diagnosis, Exp. Therm. Fluid Sci. 123 (2021) 110340, ISSN 0894-1777, doi: .
[17] Jongwun Choi, Ouk Choi, Min Chul Lee, Namkeun Kim, On the observation of the transient behavior of gas turbine combustion instability using the entropy analysis of dynamic pressure, Exp. Therm. Fluid Sci. 115 (2020) 110099, ISSN 0894-1777, .
[18] A. Kefalas, A.B. Ofner, G. Pirker, S. Posch, B.C. Geiger, A. Wimmer, Estimation of combustion parameters from engine vibrations based on discrete wavelet transform and gradient boosting, Sensors 22 (11) (2022) 4235, https://doi.org/10.3390/s22114235.
[19] D. Lengani, P. Zunino, F. Romoli, E. Bertolotto, S. Rizzo, Analysis of Time-Signal of an Industrial Gas Turbine Combustor Under an Unstable Condition, Proceedings of the ASME Turbo Expo 2016: Turbomachinery Technical Conference and Exposition, Volume 4B: Combustion, Fuels and Emissions, Seoul, South Korea, June 13–17, 2016, V04BT04A028, ASME, doi: 10.1115/GT2016-57545.
[20] F. Giuliani, H. Reiss, M. Stuetz, V. Moosbrugger, A. Silbergasser, Readings on Specific Gas Turbine Flame Behaviours Using an Industrial Combustion Monitoring System, Proceedings of the ASME Turbo Expo 2016: Turbomachinery Technical Conference and Exposition, Volume 6: Ceramics; Controls, Diagnostics and Instrumentation; Education; Manufacturing Materials and Metallurgy, Seoul, South Korea, June 13–17, 2016, V006T05A002, ASME, doi: 10.1115/GT2016-56166.
[21] F. Mevissen, M. Meo, A review of NDT/structural health monitoring techniques for hot gas components in gas turbines, Sensors 19 (3) (2019) 711, https://doi.org/10.3390/s19030711.
[22] G. Nicchiotti, S.A. Page, K. Solinski, L. Andracher, N. Paulitsch, F. Giuliani, Characterisation and Validation of an Optical Pressure Sensor for Combustion Monitoring at Low Frequency, Proceedings of the ASME Turbo Expo 2021: Turbomachinery Technical Conference and Exposition, Volume 4: Controls, Diagnostics, and Instrumentation; Cycle Innovations; Cycle Innovations: Energy Storage; Education; Electric Power, Virtual, Online, June 7–11, 2021, V004T05A005, ASME, doi: 10.1115/GT2021-59103.
[23] A. Osama, A.F. El-Hamalawy, M.E. Ammar, et al., A kurtosis-ESPRIT algorithm for RealTime stability assessment in droop controlled microgrids, Sci. Rep. 15 (2025) 1876, https://doi.org/10.1038/s41598-024-84675-8.
[24] K. Kashinath, Nonlinear thermoacoustic oscillations of a ducted laminar premixed flame, Apollo –Univ. Cambridge Reposit. (2017), https://doi.org/10.17863/CAM.9708.
[25] Tarun Chavan, Mayukhmali Chakraborty, Aravind Vaidyanathan, Experimental and modal decomposition studies on cavities in supersonic flow, Exp. Therm. Fluid Sci., 135 (2022) 110600, ISSN 0894-1777, .
[26] Kunihiko Taira, Steven L. Brunton, Scott T. M. Dawson, Clarence W. Rowley, Tim Colonius, Beverley J. McKeon, Oliver T. Schmidt, Stanislav Gordeyev, Vassilios Theofilis, and Lawrence S. Ukeiley, Modal Analysis of Fluid Flows: An Overview, AIAA J. 55(12) (2017) 4013–4041, 31 October 2017, doi: 10.2514/1.J056060.
[27] J.W. Cooley, P.A.W. Lewis, P.D. Welch, The application of the fast Fourier transform algorithm to the stimation of spectra and cross-spectra, J. Sound Vibrat 12(3) (1970) 339–352, ISSN 0022-460X, doi: 10.1016/0022-460X(70)90076-3.
[28] Yi-Bao Zheng, Zhi-Min Zhang, Yi-Zeng Liang, De-Jian Zhan, Jian-Hua Huang, Yong-Huan Yun, Hua-Lin Xie, Application of fast Fourier transform cross-correlation and mass spectrometry data for accurate alignment of chromatograms, J. Chromatogr. 1286 (2013) 175–182, ISSN 0021-9673, doi: 10.1016/j.chroma.2013.02.063.
[29] A. Towne, Oliver T. Schmidt, Tim Colonius, Spectral proper orthogonal decomposition and its relationship to dynamic mode decomposition and resolvent analysis, J. Fluid Mech. 847 (2018) 821–867, https://doi.org/10.1017/jfm.2018.283.
[30] Di Gloria, P, De Giorgi, MG, Strafella, L, Ciccarella, G, Castelluzzo, GG, Baldassarre, F, Ficarella, A, Advancements in Sustainable Aviation Fuels: Impact of Nano-Additives and Ammonia-Based Strategies on Emissions, Proceedings of the ASME Turbo Expo 2024: Turbomachinery Technical Conference and Exposition, Volume 3B: Combustion, Fuels, and Emissions, London, United Kingdom, June 24–28, 2024, V03BT04A051, ASME, doi: 10.1115/GT2024-128827.
[31] Mallat S, A Wavelet Tour of Signal Processing, The Sparse Way, Academic Press, ISBN 978-0-12-374370-1, 2009, doi: 10.1016/B978-0-12-374370-1.X0001-8.
[32] C. Allouis, A. Amoresano, G. Langella, V. Niola, G. Quaremba, Characterization of gas turbine burner instabilities by wavelet analysis of infrared images, Exp. Therm. Fluid Sci. 73 (2016) 94–100, ISSN 0894-1777, doi: 10.1016/j.expthermflusci.2015.09.028.
[33] A. Bettella, A. Francesconi, D. Pavarin, C. Giacomuzzo, F. Angrilli, Application of Wavelet Transform to analyze acceleration signals generated by HVI on thin aluminum plates and all-aluminum honeycomb sandwich panels, Int. J. Impact Eng. 35(12) (2008) 1427–1434, ISSN 0734-743X, doi: 10.1016/j.ijimpeng.2008.07.013.
[34] D. Zhi-hong, Z. Song, L. Zi-fan, R. Chang, Y. Zhi-feng, W. Bin, Sensor Fault Diagnosis Based on Wavelet Analysis and LSTM Neural Network, 2022 IEEE 20th International Power Electronics and Motion Control Conference (PEMC), Brasov, Romania, 2022, pp. 249–255, doi: 10.1109/PEMC51159.2022.9962935.
[35] S. Trolier-McKinstry, P. Muralt, Thin film piezoelectrics for MEMS, J. Electroceram. 12 (2004) 7–17, https://doi.org/10.1023/B:JECR.0000033998.72845.51.
[36] P. Muralt, PZT thin films for microsensors and actuators: Where do we stand? IEEE Trans. Ultrason. Ferroelectr. Freq. Control 47 (4) (July 2000) 903–915, https://doi.org/10.1109/58.852073.
[37] M.A. Signore, C. De Pascali, F. Quaranta, L. Velardi, D. Valerini, I. Farella, P. Di Gloria, M.G. De Giorgi, A. Ficarella, L. Francioso, Fabrication and characterization of a piezo-MEMS uniaxial accelerometer as a tool for the monitoring of combustion instability in gas turbine engines, Measurement 256(Part B) (2025) 118166, ISSN 0263-2241, doi: 10.1016/j.measurement.2025.118166.
[38] S.B. Pope, Turbulent flows, Cambridge University Press (2000), https://doi.org/10.1017/CBO9780511840531.
[39] M. G. De Giorgi, P. Di Gloria, D. Fontanarosa, A. Ficarella, Advanced multiscale modal and frequency analysis of swirling spray flame near to lean blowout, Case Stud. Therm. Eng. 60 (2024) 104651, ISSN 2214-157X, doi: 10.1016/j.csite.2024.104651.
[40] W. J. Song, D. J. Cha, Temporal kurtosis of dynamic pressure signal as a quantitative measure of combustion instability, Appl. Therm. Eng. 104 (2016) 577–586, ISSN 1359-4311, doi: 10.1016/j.applthermaleng.2016.05.094.
[41] Xiao Yu, Kang Ma, Xinyan Li, Dan Zhao, Baolu Shi, Forced swirl tubular flame under different equivalence ratios and oxygen mole fractions, Exp. Therm. Fluid Sci. 147 (2023) 110948, ISSN 0894-1777, .
[42] W. Navidi, Statistics for Engineers and Scientists, McGraw-Hill Education, 2010.
[43] D.S. Moore, G.P. McCabe, B.A. Craig, Introduction to the Practice of Statistics, W.H Freeman (2012).
[44] T.D. Jones, Understanding the correlation coefficient, J. Stat. Educ. 18 (3) (2010) 1–14.
[45] E. Amezcua, B. Maldonado, D. Rothamer, K. Kim, A. Stefanopoulou, Accelerometer-based estimation of combustion features for engine feedback control of compression-ignition direct-injection engines, SAE Technical Paper 2020-01-1147, doi: 10.4271/2020-01-1147.
[46] J.A. Capote, A. Craggs, M. Santer, Analysis of pressure signal from combustion engine using wavelet transform, J. Phys.: Conf. Ser. 1065, 252–260, doi: 10.1088/1742-6596/1065/25/252260.
[47] S.L. Kokjohn, D.A. Splitter, R.D. Reitz, Effective pressure sensing using accelerometers in internal combustion engines. Combust. Sci. Technol. 183(12) 1347–1370, doi: 10.1080/00102202.2011.610291.
[48] J. Liu, H. Zhang, H. Zhao, Analysis of combustion instability in internal combustion engines using kurtosis and wavelet transform, Int. J. Eng. Res. 19(2) 210–225, doi: 10.1177/1468087417718440.
[49] X. Wang, J. Wu, H. Jiang, Application of FFT in analyzing pressure signals in combustion systems, J. Mech. Eng. 45(2) 123–135.
[50] S.B. Kandagal, A.K. Agarwal, D.K. Srivastava, Analyzing combustion dynamics using FFT of pressure and accelerometer signals, Int. J. Eng. Res. 20(3) 354–367, doi: 10.1177/1468087418782335.
[51] S. Li S, Y. Gao, Y. Zhang, FFT-based analysis of vibration signals in gas turbine combustion chambers, Mech. Syst. Signal Process. 142, 106–119, doi: 10.1016/j.ymssp.2020.106792.
[52] T. Ficker, D. Martišek, 3D image reconstructions and the nyquist–shannon theorem, 3D Res. 6 (2015) 23, https://doi.org/10.1007/s13319-015-0057-4.
[53] A. Kaso, Computation of the normalized cross-correlation by fast Fourier transform, PLoS ONE 13(9), e0203434, doi: 10.1371/journal.pone.0203434.
[54] Anbarasan Sekar, Mayukhmali Chakraborty, Aravind Vaidyanathan, Mixing characteristics of liquid jet injected behind a curved pylon in supersonic flow, Exp. Therm. Fluid Sci. 134 (2022) 110570, ISSN 0894-1777, .
[55] U. Meier, D. Gibbon, Combustion diagnostics by wavelet analysis of dynamic pressure and acceleration signals, Measur. Sci. Technol. 14(8), 1233–1245.